

Untersuchungen zur Strahldynamik am Harmonischen Doppelseitigen Mikrotron von MAMI-C

Dissertation

zur Erlangung des Grades
„Doktor der Naturwissenschaften“

am Fachbereich Physik, Mathematik und Informatik
der Johannes Gutenberg-Universität
in Mainz

Marco Dehn

Institut für Kernphysik
Johannes Gutenberg-Universität Mainz

13. Juni 2013



Investigations on jet dynamics Harmonic double-sided microtron from MAMI-C

**Dissertation
to obtain the degree
"Doctor of Science"**

**at the Department of Physics, Mathematics and Computer
Science at the Johannes Gutenberg University
in Mainz**

Marco Dehn

Institute for Nuclear Physics
Johannes Gutenberg University Mainz

13th June 2013

Date of the oral exam: October 28, 2013

D77 – Dissertation at the University of Mainz

summary

Since 1990, the Institute for Nuclear Physics at the University of Mainz has been operating an accelerator facility for experiments in nuclear and particle physics that is unique in the world – the Mainz Microtron (MAMI-B). This accelerator cascade consists of three racetrack microtrons (RTMs) with high-frequency linear accelerators at 2.45 GHz, with which a quasi-continuous electron beam can be accelerated from up to 100 μA to 855 MeV .

In 1999, the implementation of the last stage of expansion – a harmonic double-sided microtron (HDSM, MAMI-C) – with a final energy of 1.5 GeV began. The planning required some bold steps, such as deflection magnets with field gradients and their resulting beam-optical properties, which have a major impact on the longitudinal dynamics of the accelerator. This required the introduction of the "harmonic" mode of operation with two frequencies of the two linear accelerators.

Many machine parameters (such as HF amplitudes or phases) have a direct effect on the acceleration process, but their physical quantities are not always easily accessible by measurement. In the case of an STM with a relatively simple and well-defined beam dynamics, this is not a problem in routine operation, but with the HDSM, knowledge of the physical variables is of significantly greater importance simply because of the larger number of parameters. Within the scope of this work, it was possible to develop suitable methods of beam diagnosis with which these machine parameters can be checked and compared with the planning specifications .

Since fitting the machine model to a single phase measurement does not always provide unambiguous results due to the inevitable measurement errors, a form of tomography is used. The longitudinal phase space is then examined in the form of an acceptance measurement. An extended model can then be adapted to the variety of data obtained, resulting in a greater significance of the model parameters .

The results of these investigations show that the accelerator as a whole system behaves essentially as predicted and a large number of different configurations for beam operation are possible - however, this is avoided in routine operation and a proven configuration is used for most situations. This leads to good reproducibility, for example of the final energy or the spin polarization angle at the experiment stations.

The findings from these examinations were partially automated so that the operators now have additional and helpful diagnostics available with which the machine can be operated even more reliably.

Abstracts

The Institute for Nuclear Physics at Mainz University operates a worldwide unique accelerator for experiments in nuclear and particle physics since 1990. The Mainzer Mikrotron (MAMI-B) uses three cascaded racetrack microtrons (RTM) with RF linacs operating at 2.45 GHz to accelerate a continuous electron beam of up to 100 μ A to 855 MeV.

In 1999 the realization of the fourth stage - the Harmonic Double Sided Microtron (HDSM, MAMI-C) - reaching a maximum beam energy of 1.5 GeV was started. During the development some courageous decisions were necessary. For example the bending magnets with their field gradient and corresponding beam optical properties have large influence on the longitudinal beam dynamics. That in turn requires harmonic operation with two RF linacs operating at 4.9 GHz and 2.45 GHz.

Many parameters of the machine settings (like RF voltage or phase) have great impact on the acceleration process but not always they are easily to quantify in physical units. Concerning the RTMs with their comparatively simple and well defined beam dynamics that is rather unproblematic. However, in the HDSM the larger number of parameters requires a more precise knowledge of these quantities. Therefore it is necessary to develop dedicated methods of beam diagnostics to check the important machine parameters against their design values.

All of these methods are not free of systematic errors or insufficiencies and thus fitting a model of the machine to measured data does not always yield unambiguous results. To overcome this problem a special kind of tomography is used to scan the longitudinal phase space resulting in acceptance measurements. The large amount of data with systematic variations now yields a better significance of the fitted parameters.

The results of these investigations demonstrate that the accelerator as an entity acts as predicted and shows that many different configurations can be used to operate the HDSM. However, for most situations one single configuration is established to improve the reproducibility of eg the beam energy or the spin polarization angle at the experimental areas.

Some of the resulting findings were automated to aid the operators of MAMI by means of additional diagnostic tools. These tools now guarantee a more reliable and systematic approach while operating the HDSM routinely.

Table of Contents

Part I. Of Microtrons and Polytrons	1
1 The Harmonic Double-Sided Microtron (HDSM)	3
1.1 The Mainz Microtron (MAMI)	3
1.1.1 Recirculating RF linear accelerators for relativistic particles 4	
1.1.2 The MAMI-B cascade since 1990 . 8th	
1.1.3 Extension of the cascade to MAMI-C	8th
1.1.4 The harmonic double-sided microtron (HDSM)	10
1.2 The microtron principle	13
1.2.1 Coherence Conditions for Relativistic Energies	13
1.2.2 Higher energies with MAMI-C	14
1.3 The deflection system and its properties	15
1.3.1 Focusing the Beam	17
1.3.2 Longitudinal Focusing	20
1.4 Periodic Systems: Fundamentals of Longitudinal Dynamics	21
1.4.1 Description by the linear beam dynamics.	21
1.4.2 Matrix Formalism of Jet Dynamics	22
1.4.3 Stability, Eigenellipse and Resonance Phenomena . . . 24	
1.4.4 Influence of the magnetic field gradient on the longitudinal dynamics. 28	
1.4.5 Longitudinal Stability of the DSM . . 29	
1.5 The Harmonic Double-Ended Microtron as a Special Case for MAMI-C 31 . 29	
1.5.1 Subharmonic margin	
1.5.2 Longitudinal stability of the HDSM	32
1.5.3 Consequence of the target phase change in the HDSM.	32
1.5.4 Consequences in operation and for jet dynamic investigations . . . 34	
1.5.5 Coupling between the phase spaces	35
Part II. Beam diagnostics and other systems at MAMI	37
2 Beam Diagnostics and Other Systems at MAMI 2.1	39
Invasive Monitor Systems	41
2.1.1 Fluorescent screens	41

Table of Contents

2.2 Non-Invasive Monitor Systems	43
2.2.1 Synchrotron Radiation Monitors	43
2.3 Various diagnosis systems	43
2.3.1 Förster probe for current measurement.	44
2.3.2 Ionization probes monitor beam losses.	44
2.4 High Frequency System	45
2.4.1 Accelerating Voltage	45
2.4.2 Phase Shifter	47
2.4.3 Autodyne phase measurements	51
2.5 Magnetic Field Measurements	52
2.6 High Frequency Monitors	53
2.6.1 Basics	53
2.6.2 Various functions of the HF monitors	54
2.6.3 Analog signal processing	55
2.6.4 HF monitors in the recirculating accelerator	56
2.6.5 Data Collection	58
2.7 Data processing.	62
2.7.1 Interpretation and Analysis of the Signals	62
2.7.2 Archiving of the ADC raw data	63
2.7.3 Data Acquisition Performance	64
 Part III. Elementary processes and methods	 67
 3 Elementary processes and methods	 69
3.1 Phase measurements with HF monitors in the microtron	70
3.1.1 Phase Monitors in the RTMs	70
3.1.2 Phase Monitors in HDSM	71
3.2 Elementary Methods for Phase Measurements in HDSM	72
3.2.1 Precise phase measurement with waveguide phase shifters	73
3.2.2 Determination of the Bullet Phases	73
3.3 Calibration of the phase monitors	75
3.3.1 Requirements for an automatic measurement routine.	76
3.3.2 Improved analysis with phase and intensity signal (simultaneous)	76
3.3.3 Improved signal analysis of the ADC raw data	78
3.3.4 Fast phase measurements with individual diagnostic pulses	81
3.4 Examination of the Linacs	81
3.4.1 Measurement Methods	84
3.4.2 Results	88
3.5 Calibration of the position monitors of the HDSM	91

3.6 Flexible measurement methods	94
3.6.1 Examination of the phase measurement in the RTMs	94
3.6.2 Determining the phase in the matching and vernier sections of MAMI-B	94
3.6.3 Use in beam position control before the A4 experiment . .	94
3.7 Results of the investigations	94
Part IV. Beam Dynamics	97
4 Jet dynamics 4.1	99
Investigation of the longitudinal dynamics of the HDSM	99
4.2 Longitudinal Dynamics in HDSM	101
4.2.1 Model of longitudinal dynamics . . 103	
4.2.2 Implementation of the longitudinal jet dynamics model. . 104	
4.2.3 Adaptation of the model 106	
4.3 Phase space tomography as a basis for further investigations.	109
4.3.1 Acceptance Measurements as Phase Space Tomograms	110
4.3.2 Phase measurements during acceptance measurement	112
4.3.3 Optimization of the simulation parameters (Fit)	115
4.4 Results of the model	121
4.4.1 Simulation of scrap energy	122
4.4.2 Stability of the Spin Angle	124
4.5 Analysis of synchrotron oscillations	125
4.5.1 The progression of the working point in the HDSM.	126
4.5.2 Determination of the synchrotron oscillation from the phase curve. 129	
4.5.3 Evaluation of the synchrotron oscillation 131	
4.5.4 Acceptance Measurements and Synchrotron Oscillations	133
4.5.5 Stability of Longitudinal Dynamics	133
4.6 Optimizations of the accelerator in beam operation	134
4.6.1 Optimization with phase space tomograms	136
4.6.2 Phase optimization using synchrotron oscillation.	136
4.7 Results of the jet dynamic investigations	138
Part V. Summary and Outlook	141
5 Summary and Outlook 5.1 Summary . .	143
.	143
5.2 Outlook	145

Table of Contents

Part VI. Appendix	147
List of Figures	149
List of Tables	151
index	153
bibliography	155
publications	163
thanksgiving	165

Icon Directory

symbol	explanation	Unit
q, e	Charge, elementary charge	[c]
m, m_0	Mass, rest mass	[kg]
t, T_i	Time, point in time of a revolution	[n]
$u(t) \tilde{y}$	Voltage of the time-dependent signal	[V]
$\tilde{y} =$	frequency (as specifications)	[\tilde{y}]
$\tilde{y}_1 \tilde{y}_2$	Static phase shift between two linacs	[\tilde{y}]
\tilde{y}	Measured phase (e.g. with phase monitors)	[\tilde{y}]
\tilde{y}	Phase advance of the synchrotron oscillation	[\tilde{y}]
$q = \tilde{y}/2\tilde{y}$	point ("tune") of the synchrotron oscillation	
AS	Amplitude of the synchrotron oscillation	[\tilde{y}]
\tilde{y}_0	Initial phase of the synchrotron oscillation	[\tilde{y}]
x, y, z	Cartesian coordinates (co-moving coordinate system)	[m]
$x\tilde{y}, y\tilde{y}, z\tilde{y}$	Impulses in Cartesian coordinates (moving coordinate system)	[mrad]
R	Radius of a circular path	[m]
\tilde{y}	deflection angle	[\tilde{y}]
c	speed of light	[m/s]
v	speed in units of c	[m/s]
$\tilde{y} = v/c$		
$\tilde{y} = \tilde{y}_1 \tilde{y}_2 \tilde{y}_1$	relativistic Lorentz factor	
	Wavelength of the radio frequency	[m]
$\tilde{y}\tilde{y}, f$	frequency of high frequency	[GHz]
\tilde{y}	angular frequency	[Hz]
\tilde{y}	period of high frequency	[n]
n	efficiency	[%]
k	wavenumber	[1/m]
i	jet stream	[A]
i, j, k	number of a round	
B	Magnetic field	[T]
$E, \tilde{y}E, \tilde{y}E$	Energy, energy gain, energy variation	[MeV/c ²]
U_0	Peak voltage (also amplitude) of the linac	[MV]
L	Total length of the linac	[m]
	Quality of a resonator (unloaded / loaded)	
$r_{\text{Shunt}} = Q/Z$	shunt impedance of a resonator	[M \tilde{y} /m]
Z	impedance of an oscillating circuit	[\tilde{y}]
k	coupling constant	
P	Output	[W]
$p, \tilde{y}p, \tilde{y}p$	pulse	[MeV/c]
N	Number of linacs or deflection systems (polytron)	
n	harmonic number of the microtron	
M, D, L	different transfer matrices of the longitudinal beam dynamics	
$M\tilde{y}$	accelerator model	
$k, \tilde{y}\tilde{y} k$	Accelerator configuration, configuration change	

List of abbreviations

Abbreviation meaning	side
MAMI Mainz Microtron	3
RTM race track microtron	3
DSM Double Sided Microtron	4
HDSM Harmonic double- sided microtron	29
DBM "double balanced mixer" (HF mixer)	55
HF High -frequency	4
Linac linear accelerator	3
CW "continuous wave" (continuous wave)	7
DC direct current	56
DAC "digital analog converter"	39
ADC "analogue to digital converter"	58
LM Levenberg-Marquardt algorithm	117
PSO "Particle Swarm Optimization"	118

Part One.

Of microtrons and polytrons

Microtron, electron cyclotron, an electron accelerator similar to the ion cyclotron for energies up to about 30 MeV. The electrons travel in a vacuum chamber between the poles of a constant magnetic field on circular paths that touch tangentially at one point. At the point of contact of the circular orbits they are driven by the strong electric field of a microwave cavity accelerated.

Since the speed of the electrons at these energies is close to the speed of light, the orbital period changes with the energy and the orbit radius, in contrast to the ion cyclotron. Therefore, the increase in energy per revolution must be chosen so that the increase in revolution time is a multiple of the period of the microwave oscillation. Stability is achieved when the increase in energy is in turn a multiple of the rest mass of the electron. In 1944 the principle was described by V. Veksler and in 1948 the first M. by WJ Henderson, H. Le Caine and R. Montalbetti built.

Brockhaus Encyclopedia, 17th Edition, Volume 12, 1971

Cavity resonator, an oscillating circuit for electromagnetics used in high-frequency technology.

Vibrations of very high frequency, in the simplest case a cylindrical metal can closed on all sides. You can think of it as being caused by the rotation of an ordinary oscillating circuit consisting of two parallel circular plates (capacitor) and a wire bracket (coil) around the line connecting the center points of the circle.

Brockhaus Encyclopedia, 17th Edition, Volume 8, 1971

See first, think later, then test.
But always see first.
Otherwise you will only see what
you were expecting.
Most scientists forget that.

(Douglas Adams)

1 The Harmonic Double Faced Microtron (HDSM)

The fascinating success story of the Institute for Nuclear Physics in Mainz goes back to the 1960s, when the pulsed 300 MeV linear accelerator (Linac) went into operation here [1]. Since then, major international successes have been achieved in the fields of nuclear and particle physics as well as in the field of accelerator physics, since the accelerator facility has been continuously developed to meet the requirements of the experiments [2, 3].

For the study of matter and the fundamental forces of physics, the electron is valued as an electromagnetic probe because it can be viewed as a point particle in experiments. In contrast to hadrons, where the individual momenta of the partons have to be taken into account in high-energy collisions, the entire energy E_{e} of the electron can go directly into the collision. Therefore, investigations with an electron beam are usually easier and more precise to analyze compared to hadron beams.

1.1 The Mainz Microtron (MAMI)

In Mainz, as early as the 1970s, researchers were investigating the possibility of generalizing the racetrack microtron (RTM), consisting of *an* acceleration section and two 180° deflection magnets, to *several* acceleration sections and pairs of deflection magnets in order to produce a continuous electron beam with energies well above 1 GeV for experiments of nuclear and particle physics. Beam intensities of up to 100 μA are aimed at in order to achieve high efficiency in fixed-target experiments. The generalized term *polytron*¹ should be used for such multi-sided microtrons with “really many” magnets [5];

¹In fact, the term “polytron” in connection with plasma research and nuclear fusion was coined as early as 1961 by MG Haines (“Experiments on the Polytron, a toroidal Hall accelerator employing cusp containment”) for the generation of a plasma [4].

1 The Harmonic Double-Sided Microtron (HDSM)

the double-sided microtron (DSM, $N = 2$ for two straight segments) was initially called "bicyclotron" [6], the next higher orders would be "hexatron" ($N = 3$ straight segments) or "octotron" ($N = 4$). Figure 1.1 schematically shows the first representatives of the polytrons.

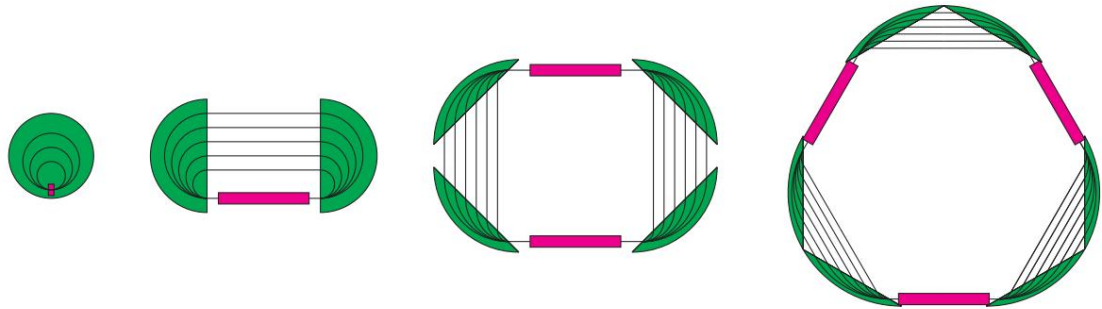


Figure 1.1:

Family of microtrons: "classic" microtron, RTM, DSM, hexatron. magnets are green
HF linacs shown in purple and recirculation lanes in black (not to scale).

The fundamentally simple structure of the microtron means that just a few fundamental relationships already provide a good overview of the possibilities of the respective accelerator [5, 7]. These relationships are summarized in the following sections to understand the difficulties that were detailed during the planning. This gives rise to various questions, which are examined from Chapter 2 onwards. Chapter 3 shows how fundamental measurement results are combined to obtain additional information. In Chapter 4 in particular, the results are compared with the parameters chosen during the planning phase.

Normally, the behavior of the target particle, which crosses the accelerator on the target path, is examined. The particle experiences the target energy gain $\ddot{y}E_{\text{Soll}}$ because it reaches the acceleration distance at the target phase \ddot{y}_{target} . All other particles are characterized in the linear beam dynamics by their deviations (e.g. $\ddot{y}E$, $\ddot{y}\ddot{y}$ or similar).

1.1.1 Recirculating RF linear accelerators for relativistic particles

The racetrack microtrons (RTM for *race track microtron*) based on an idea by Schiff [8] combine high-frequency linear accelerators (linac) with the recirculation of the relativistic electron beam through a suitable deflection magnet system. The beam can be accelerated multiple times through the linac by the energy gain $\ddot{y}E = eU_{\text{Linac}} \cdot \cos(\ddot{y}S_{\text{oll}})$ if the recirculation flight time is an integer multiple of the accelerating HF period $\ddot{y} = \ddot{y}_{\text{HF}}/c \cdot U_{\text{Linac}}$ (usually referred to as U_0 in the following) is the maximum voltage of the linac and $\ddot{y}S_{\text{oll}}$ is the target phase of the beam

1.1 The Mainz Microtron (MAMI)

relative to the maximum HR. Since an RF linac is used, the accelerated beam cannot be continuous, but will consist of individual packets (bunches) whose maximum repetition rate usually corresponds to the RF used.

Among various other recirculating linear accelerators, the STMs play a special role: Despite the comparatively simple recirculation using two 180° deflection magnets, the inherent phase focusing (Figure 1.2 and Section 1.4) of such recirculators automatically compensates for fluctuations in the energy gain γE , since the longitudinal dispersion of the deflection system the flight time of a revolution for relativistic particles is proportional to their energy [9]. As a result, fluctuations in the energy gain do not affect the final energy as a sum, but are reduced by the number of recirculations, so that a microtron with a few recirculations will ideally have a significantly lower fluctuation in the final energy than a linac of comparable energy.

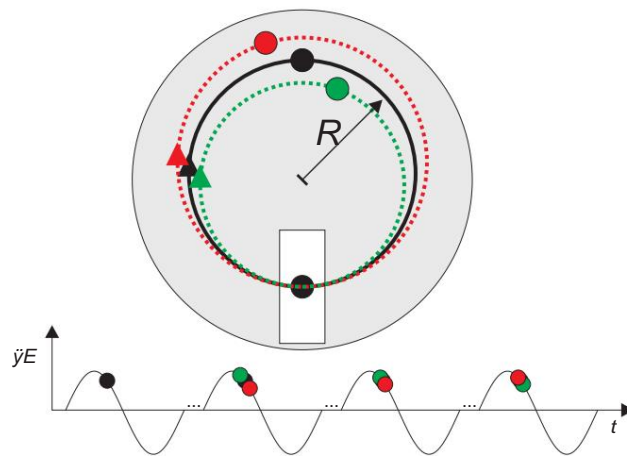


Figure 1.2:

Longitudinal focussing (phase focussing) in the "classic" microtron: In the longitudinal plane, too, the phase focussing by magnetic field (grey) and acceleration (white) ensures that particles with energy errors $\gamma\tilde{E}$ (red) and $\gamma\tilde{E}$ (green) reach the HF resonator later or earlier than the target particle (black). If the phase of the HF is selected in such a way that the target particle sits on the falling edge of the electric field, the energy deviations $\gamma\tilde{E}$ are compensated for within a few revolutions.

Because the electrons are already relativistic at low energies and the speed increases only slightly, a single RF linear accelerator can be used to accelerate different energies *simultaneously*².

²The phase speed of the accelerating high frequency v_P must correspond to the speed of light. The target phase $\gamma\tilde{E}_{\text{Soll}}$ then remains practically constant during a linac passage.

1 The Harmonic Double-Sided Microtron (HDSM)

Main features: deflection system and linear accelerator

The essential features of the racetrack microtron are two normally homogeneous 180° deflection magnets (one can imagine the "classic" microtron divided in the middle) and an HF linac, which provides the required energy gain for the relativistic particles (Figure 1.3). As early as 1967, it was proposed to use STMs to generate a continuous high-energy electron beam for precision experiments [10].

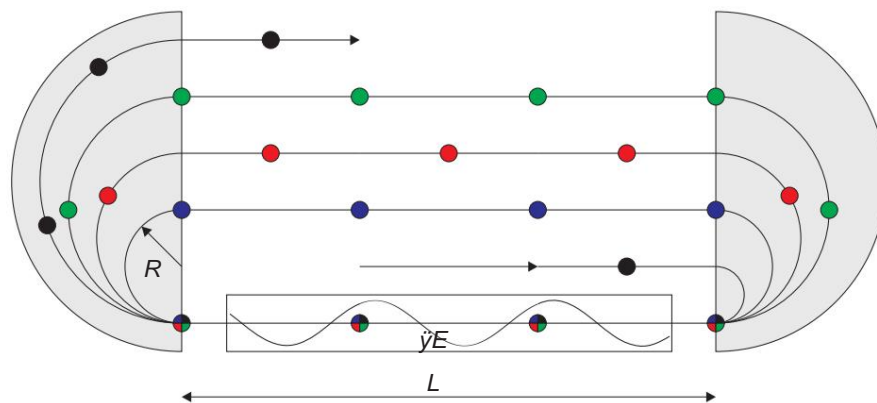


Figure 1.3:

Racetrack microtron (RTM): The magnets (grey) direct the beam or the bunches (injection, black circles) by 180° into the linac. After the acceleration by $\vec{y}E$, the deflection radius \vec{y} is larger (blue bunches), etc. The distance \vec{y} between the deflection systems can be used for the linac and focusing elements.

High energies require microtron cascade

In order for the electrons in the linac to be accelerated with each pass, they must always arrive in the resonator with the correct phase \vec{y} (coherence condition, Section 1.2.1). For this, the flight time must be an integer multiple of the HF period duration THF .

The cyclotron frequency f_Z corresponds to the rotation frequency of the first rotation and thus to the minimum HF accelerator frequency in the "classic" microtron. It links energy $E = \vec{y}m_0c^2$ (rest mass m_0) and magnetic field B :

$$f_Z = \frac{1}{2\vec{y}} \cdot \frac{q}{B\vec{y}m_0} \quad (1.1)$$

With a magnetic field of 1 T, a cyclotron frequency of 28 GHz results for $\vec{y} = 1$. Two conclusions can be drawn from this:

1. "Slow" electrons ($\vec{y} < 10$) can only be meaningfully accelerated in the classic microtron with magnetic fields $B \vec{y} 0.1$ T in order to avoid high frequencies in the technically

1.1 The Mainz Microtron (MAMI)

being able to use the easily controllable S-band range (2-4 GHz); However, high energies are uneconomical with low magnetic fields because of the large bending radii.

2. On the other hand, highly relativistic electrons ($\gamma \gg 10$) can also be accelerated with S-band technology, but now with magnetic fields of 1 T or more.

Taken together, both conclusions justify the construction of a cascade of microtrons to reach higher energies [11]. With the same acceleration frequency³ in the cascade, the magnetic fields of each stage are selected to match the respective energy range.

high frequency accelerator

The parameters total length L , energy gain γE and operating frequency γ of the linac can be flexibly adapted to local conditions. Normally conducting cavity resonators with an unloaded Q_0 of 103 to some 104 at frequencies in the S-band are used, acceleration gradients of some 10 MV/m and more (pulsed) and around 1 MV/m (CW) can be achieved and only through the available HF power or cooling is limited, since a large part of the PHF power is dissipated in the resonators [7, 12, 13].

With the shunt impedance⁴ r_{Shunt} , the maximum acceleration voltage of a acceleration section can be calculated as a function of the coupled RF power:

$$U_0 = \gamma n_{\text{acc}} / 2 \gamma_{\text{HF}} r_{\text{Shunt}} \text{PHF} \quad (1.2)$$

n_{acc} . the number of acceleration cells. In the case of the MAMI sections, r_{Shunt} is around 70 M Ω /m at 2.45 GHz and around 80 M Ω /m at 4.9 GHz. With a length of around 1 m and $n_{\text{acc}} = 35$, a power of around 15 kW is required for an energy gain of 1 MeV from the 4.9 GHz sections. Both the 2.45 GHz and 4.9 GHz klystrons deliver between 50 kW and 60 kW output power. The performance is ideal for a two meter long 2.45 GHz section or two 4.9 GHz sections

to supply.

If a beam current of 100 μA is to be accelerated with a linac, the efficiency $\gamma = P_{\text{beam}}/\text{PHF} \approx 100\text{W}/15\text{ kW}$ of these normally conducting structures is very small. It is therefore much more economical if the beam traverses the structure multiple times.

³The bunch repetition frequency γ_{Bunch} of the first stage determines the minimum frequency of all following stages.

Only integer multiples $k \cdot \gamma_{\text{Bunch}}$ of this frequency can be used in the cascade.

⁴With the relationship $U_0 = \gamma^2 P_{\text{HF}} r_{\text{Shunt}}$, at resonance the shunt impedance r_{Shunt} , which is determined by the geometry of a resonator, links the coupled power PHF with the peak voltage U_0 of the individual resonator [14].

1 The Harmonic Double-Sided Microtron (HDSM)

1.1.2 The MAMI-B cascade since 1990

The era of the pulsed linear accelerator in Mainz came to an end in 1989. More than a decade earlier, it was decided to set up a microtron cascade of three STMs that would reach an energy of 855 MeV at a beam current of 100 μA [11, 15]. The STMs, which were set up in two expansion phases, proved to be very reliable and delivered excellent beam quality: final energies of up to 855 MeV and beam intensities of up to 100 μA at 85% polarization are available in routine operation for experiments in nuclear and particle physics [16-18]. Figure 1.4 shows the current floor plan of the accelerator facility.

High beam quality of the microtron cascade

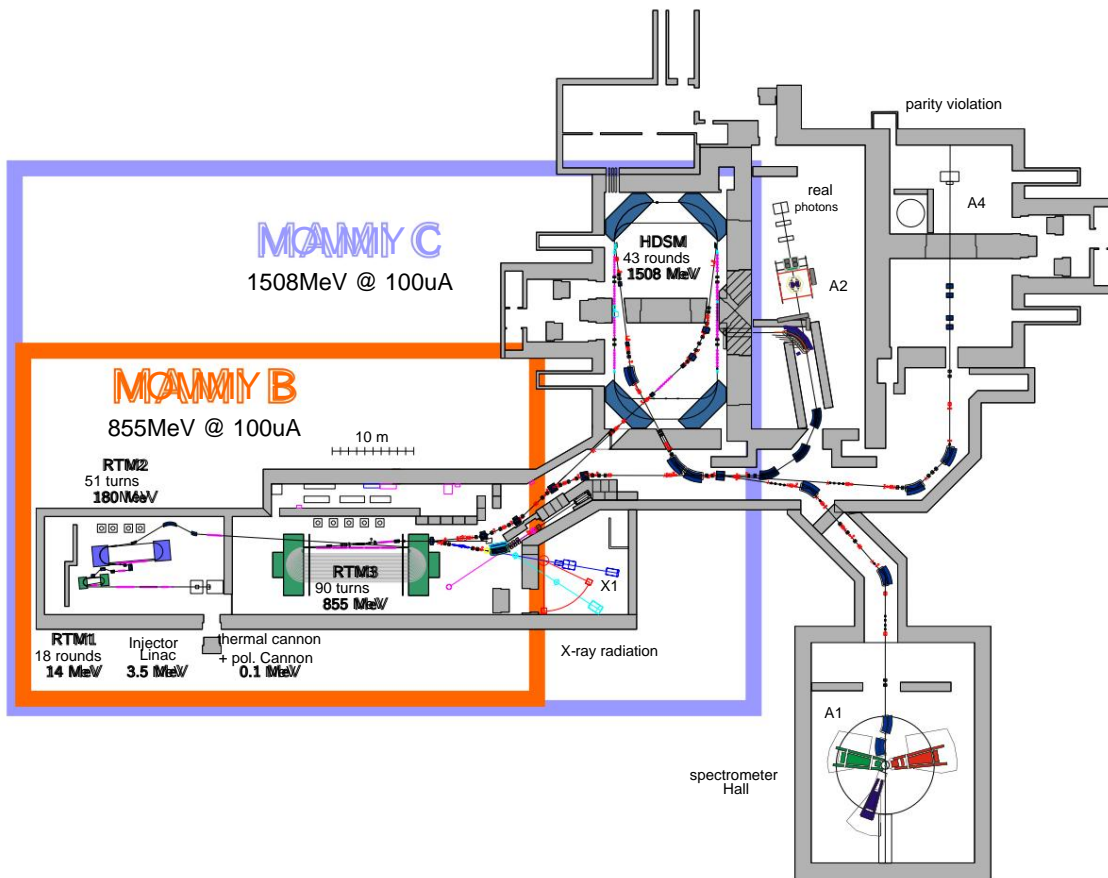
The absolute energy of the beam can be determined with an accuracy of ± 160 keV by very precisely measuring the bending radius in the known magnetic field of the RTM3 bending magnet [19]. In addition, the natural relative fluctuations $\delta p/p \approx 10^{-4}$ can be reduced to almost $\delta p/p \approx 10^{-6}$ by measuring the energy-dependent flight time of the extracted beam through the RTM3 bending magnet using two RF phase monitors (see Chapter 2) and is stabilized accordingly [20].

The natural pulse width is about $\delta p \approx 12$ keV at 855 MeV, which is essentially caused by the stochastic emission of synchrotron radiation quanta in the RTM3.

1.1.3 Extension of the cascade to MAMI-C

However, the production threshold of some mesons and hyperons of nuclear physics interest requires a higher beam energy than that of MAMI-B. From around 2 GeV, the electron stretcher facility (ELSA) in Bonn could be used for complementary experiments. However, such a synchrotron is not suitable for some of the planned experiments (eg intensities over 1 μA , parity violation). Therefore, in 1999 the decision was made to increase the energy from 855 MeV to around 1.5 GeV within the framework of the newly founded Collaborative Research Center 443 of the DFG ("Many body structure of strongly interacting systems") in order to close this gap. Here, too, the proven technology of MAMI was essentially used (ie no technological innovations such as superconducting high-frequency structures or magnets) in order not to impair the good beam quality and reliability of MAMI, even at the highest energies.

1.1 The Mainz Microtron (MAMI)

**Figure 1.4:**

Floor plan of the MAMI accelerator facility: MAMI-B started operations in 1990-1991 in the buildings specially built for this purpose. The beam guidance from RTM3 and the spectrometer hall were set up in parallel. The other parts of the building (HDSM, A2 and A4) date from the time of the Mainz linear accelerator and were used as experimental sites before MAMI-C. The high cost of a new, separate HDSM building led to the HDSM being constructed in two of these experimental halls (originally X1 collaboration). The X1 collaboration, in turn, moved to the smaller loading hall, which is directly adjacent to the RTM3. For all other experiments (A1, A2 and A4) all energies that can be reached with MAMI-C have been available since 2007.

1 The Harmonic Double-Sided Microtron (HDSM)

No RTM4

Various arguments speak against another RTM: Because of the large magnet mass⁵, the accelerator would be comparatively expensive; In addition, the relatively small energy gain means a correspondingly high number of recirculations, which above 1 GeV would also mean strongly increasing synchrotron radiation losses and an increase in the energy range.

A double-sided microtron requires only a fraction of the magnet mass compared to a comparable microtron (i.e. same magnetic field), mainly because the beam penetrates less deeply into the magnet and the pole area becomes smaller overall [7]: The magnetic area of the STM is πR^2 , for a double-sided one a microtron results in $(\pi/2)R^2$, for a hexatron $(\pi/2 \cdot 3/2)R^2$ etc., where R is the bending radius of the last revolution.

The relative saving effect on the pole face is greatest from $N = 1$ to $N = 2$, which is shown schematically in Figure 1.5.

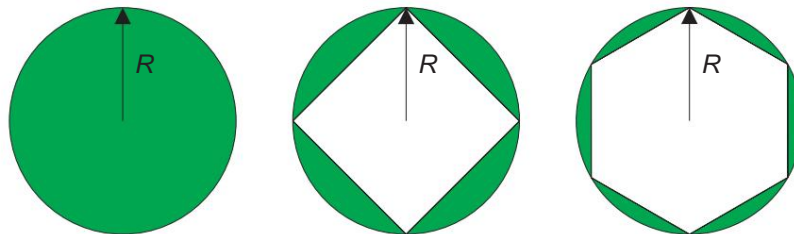


Figure 1.5:

Pole area of different types of microtrons: The pole area for a given magnetic field \vec{y} and energy $\vec{y}\vec{y}\vec{y}$ is largest for the classic microtron ($\vec{y} \vec{y} \vec{y}$) with $\vec{y}\vec{y}\vec{y}$ and decreases with increasing \vec{y} .

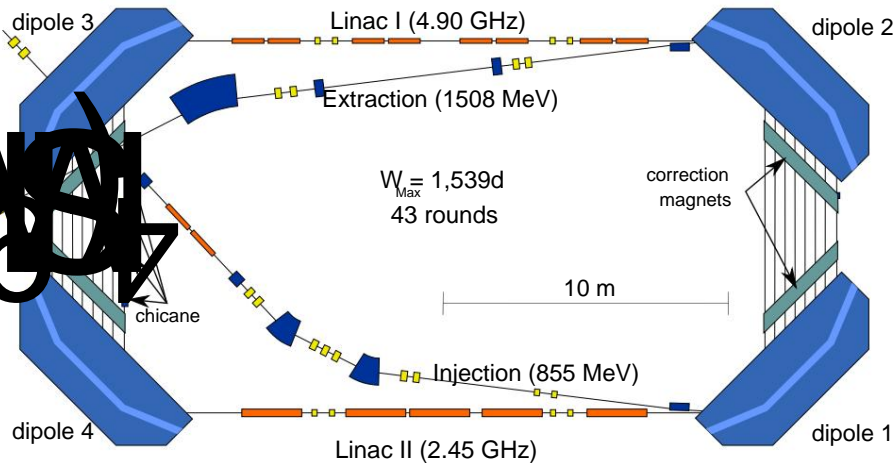
1.1.4 The harmonic double-sided microtron (HDSM)

The HDSM (Figures 1.6 and 1.7) is adapted to the special situation at MAMI:

- The accelerator fills the entire available space of two former experimental halls (see Figure 1.4).
- The transversal focusing can be realized with quadrupole magnets on the linac axes, as with the STMs, because the ratio between exit and injection energy is only 1508 MeV / 855 MeV, much lower than with all previous MAMI STMs.

⁵With a constant magnetic field, the magnetic mass scales almost with E^3 , so it would be from the RTM3 with 2x450 t to the RTM4 with 2x3000 t increase drastically.

1.1 The Mainz Microtron (MAMI)

**Figure 1.6:**

Schematic of the HDSM: After the injection (energy matching with the matching section), two linacs (4.9 GHz and 2.45 GHz, section 1.5) accelerate the electrons. Correction magnets (each two pairs h/v) on the dispersive return paths direct each orbit centered through the following linac.

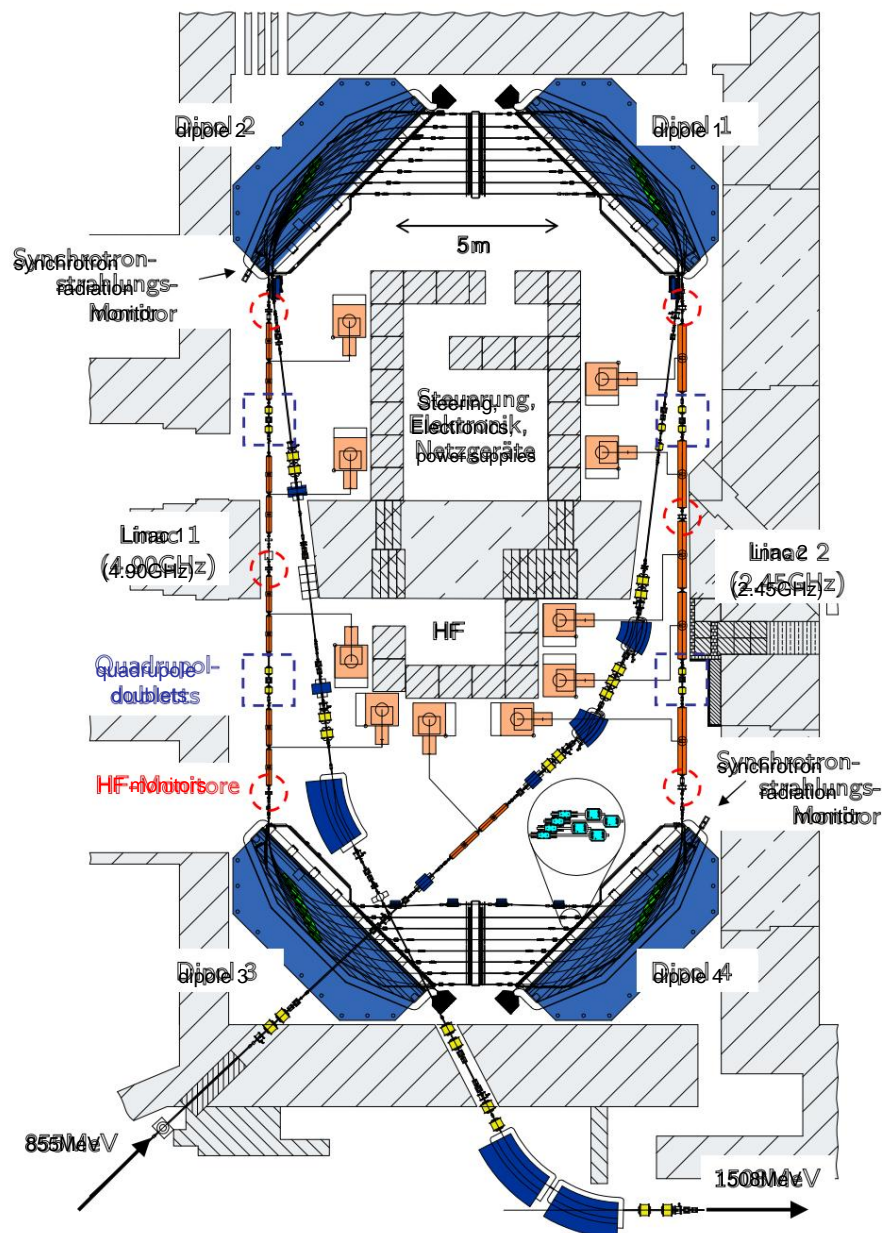
The four magnet "chicane" in the first loop between dipoles 3 and 4 lengthens the running distance to complete the longitudinal adjustment (Section 1.4.3).

The most important solution approaches of the HDSM are listed here:

- Fundamental frequency at 4.9 GHz to reduce the energy gain (section 1.2.2) • Innovative focusing scheme thanks to the field gradient of the dipole magnets to avoid the vertical master phase space (Section 1.3.1)
- This results in a migration of the target phase γ_{target} from cycle to cycle (Ab section 1.4)
- Longitudinal stability problems can be avoided by the 2.45 GHz linac (Linac II), since with subharmonic injection in a linac only every second resonator is occupied - hence the term *harmonic* DSM (Section 1.5, Figure 1.8)

In order to be able to understand how this new accelerator works, the difficulties that had to be taken into account in the design are explained in the next few sections. The RTM is often used here, which makes it easier to see some problems.

1 The Harmonic Double-Sided Microtron (HDSM)

**Figure 1.7:**

Ground plan of the HDSM: beam diagnosis (intensity, phase, as well as \ddot{y} and \ddot{y}) for all orbits is realized with the HF monitors on the linac axes (red markings, details in Section 2.6), and focusing is also done exclusively with four quadrupole doublets (yellow) on the linac axes. With the 2.45 GHz linac, one klystron supplies each acceleration section; with the 4.9 GHz linac, the power of each klystron is distributed over two sections. The synchrotron monitors are used to examine the transverse properties of the beam.

In the enlarged section at dipole 4, the arrangement of the correction magnets (turquoise) on the dispersion paths is shown as an example.

1.2 The microtron principle

The basic idea behind the microtron is to use an acceleration structure (or Linac) to traverse several times and thus to use more efficiently⁶. In particular with normally conducting acceleration structures, the efficiency $\tilde{\gamma} = P_{\text{Beam}}/P_{\text{HF}}$ is too small to economically accelerate a continuous electron beam in the GeV range.

The core components of the microtron are the acceleration structure and a deflection system common to all energies, which first separates the beams of different energies and later directs them back into the accelerator axis in phase.

The simplest example of this is the "classic" microtron (see Figure 1.2): The homogeneous magnetic field perpendicular to the accelerator level allows the electrons of different energies to return to the common starting point, where the HF resonator for acceleration is located at the same time.

The generalization of this principle replaces the circular deflection magnet of the recirculation by $2 \times N$ pairs of deflection magnets with deflection angle $180^\circ/N$. Due to the arrangement in pairs, the rays are also directed onto a common axis after passing through a pair of magnets [5].

1.2.1 Coherence conditions for relativistic energies

With the microtron ($\tilde{\gamma} \gg 1$), the flight time of a recirculation depends on the energy γ . Essentially determined by the increasing orbit radius (transversal dispersion):

$$R = \frac{\tilde{\gamma} E_0}{e c B_0} \quad (1.3)$$

This resulting change in flight time is the longitudinal dispersion.

As early as 1944, Veksler published the following simple concept for accelerating relativistic particles ("classic" microtron):

1. The flight time of the first recirculation at energy E_0 must be an integer multiple ($m \gg N$) of the accelerating high-frequency period (static coherence condition, equation 1.4).
2. The flight times of the next recirculations at the energies $E_i = E_0 \tilde{\gamma}_i + \tilde{\gamma} E$ must increase by an integer multiple ($n \gg N$) of the accelerating high-frequency period (dynamic coherence condition, harmonic number n , equation 1.5).

⁶Compared to a linac with the same beam energy and intensity, the cost savings in the Purchase and operation can be significant.

1 The Harmonic Double-Sided Microtron (HDSM)

This corresponds to the two relations (for $\gamma = 1$):

$$2\gamma \frac{E_0}{e c B \gamma E_-} = m^* \gamma_{HF} \quad (1.4)$$

$$2\gamma e \frac{--}{c B_{--}} = n^* \gamma_{HF} \quad (1.5)$$

The minimum energy gain to be applied is thus determined solely by the selection of the magnetic field B and the HF wavelength γ_{HF} . With two deflection systems consisting of for every two 90° deflection magnets, the relations change for a complete revolution based solely on the arrangement of the magnets as follows:

$$2 (\gamma \gamma^2) \frac{\gamma E}{e c B} = n^* \gamma_{HF} \quad (1.6)$$

The minimum energy gain of such a "unilateral" double-sided microtron is thus almost three times ($2\gamma/2(\gamma \gamma^2)$) larger than that of an RTM. Will one Mikrotron equipped with *two* linacs, the coherence conditions for both half Circuits apply simultaneously, so that the path length change of an entire circuit now must be at least 2γ :

$$2 (\gamma \gamma^2) \frac{\gamma E}{e c B} = 2n^* \gamma_{HF} \quad (1.7)$$

Thus, although the pole area of a double-sided microtron is drastically reduced, but two linacs must provide at least five times the energy gain compared to an RTM.

In principle, the smallest possible energy gains are preferred in CW operation (i.e. $n = 1$); but in order to build the accelerator as compact as possible at the same time, this has to be done magnetic field be as large as possible.

1.2.2 Higher energies with MAMI-C

MAMI-C was to be set up in two halls previously used as an experimental area, to save costs for a new building (see figure 1.6). Because conventional Magnets with a large homogeneous pole area ($\gamma B/B \sim 10^4$) maximum fields of about 1.5 T achieve, the energy gain of a double-sided microtron according to equation 1.7 be around 40 MeV at the MAMI frequency of 2.45 GHz.

Consequence for MAMI-C

Both linacs would therefore have to have a maximum acceleration voltage of $U_0 \sim 25$ MV provide - with about 12 m available length.

The energy gain according to equation 1.7 is proportional to γ_{HF} , so it can be given by the selection of the acceleration frequency and thus γ_{HF} can be influenced. The MAMI-B cascade as a pre-accelerator delivers a beam with a 2.45 GHz structure, so that

1.3 The deflection system and its properties

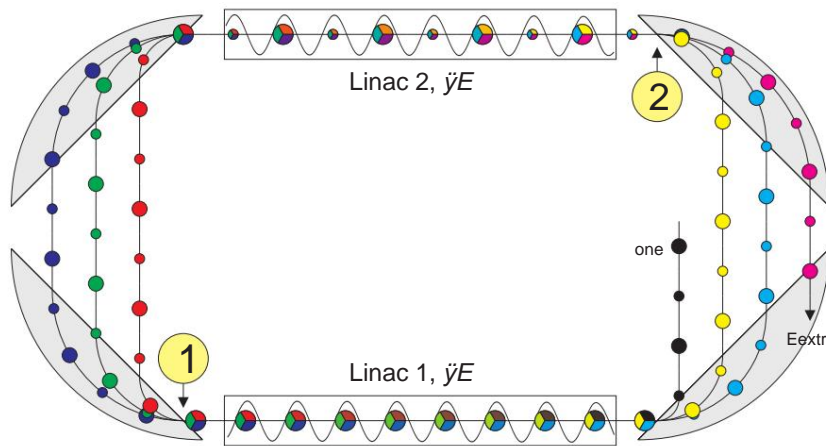


Figure 1.8:

Double-sided microtron (DSM): Schematic representation with electron bunches. From (1) to (2) the distance λ , from (2) to (1) is already 2λ long, since the beam energy is already greater than from (1) to (2). The first round is therefore 3λ long. From (1) to (2) the route is now 2λ long, exactly 1λ longer than in the first round, from (2) to (1) now 3λ . Thus, the second wrap is 5λ long, 2λ longer than the first wrap, as required by Equation 1.7. Every second bunch is shown smaller because with MAMI-C (4.9 GHz) only every second bunch (2λ 4.9 GHz) is occupied. Therefore, in the case of λ the bunches are separated by λ on one linac line and by 2λ on the other. The length of the first circuit (even/odd) determines which bunch spacing will be on which linac straight. In principle, this enables operation with two 4.9 GHz linacs (DSM) as well as mixed operation (4.9 GHz and 2.45 GHz linac, harmonic DSM, Section 1.5).

initially all integer multiples of this frequency come into consideration. Because the dimensions of the acceleration structures scale with the wavelength, 4.9 GHz for the DSM is a good compromise between energy gain on the one hand and production, adjustment and, above all, aperture on the other. Figure 1.8 schematically shows the special situation with MAMI-C, which arises due to the differences in the bunch frequency and fundamental frequency of the DSM. Further details can be found in [21], for example.

1.3 The deflection system and its properties

The recirculation can be realized by segment magnets, each with common entry and exit edges (see Figure 1.9), since such a magnet has telecentric imaging properties in the deflection plane for reasons of symmetry and therefore acts like a magnetic mirror. The deflection angle remains energy-independent; only the bending radius and thus the exit point scales as transversal

1 The Harmonic Double-Sided Microtron (HDSM)

dispersion with the energy. The symmetrical combination of two magnets of the same kind exactly reverses this effect of the single magnet, so that the transverse dispersion vanishes after such a deflection system and the trajectories of all energies are reunited [6]. The deflection angle of both magnets must be the same. It makes sense to use deflection angles of twice $\tilde{\gamma} = 180\tilde{\gamma}/N$, where N is the number of deflection systems with pairs of magnets or straight sections with dispersion $D = 0$. Possible are $180\tilde{\gamma}$ (RTM, $N = 1$), $90\tilde{\gamma}$ (DSM, $N = 2$), $60\tilde{\gamma}$ (Hexatron, $N = 3$) etc.

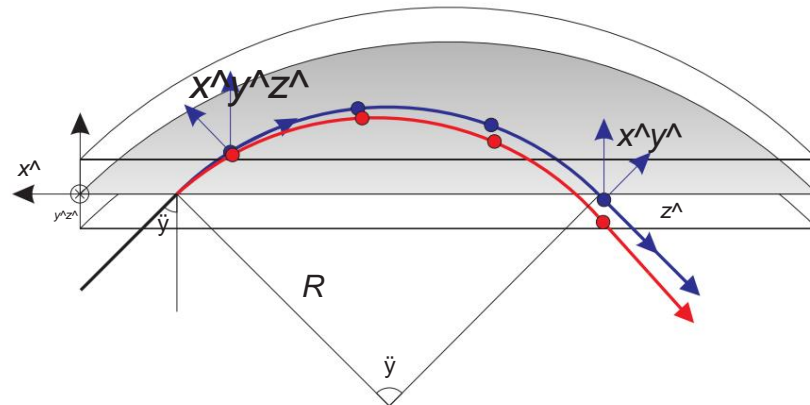


Figure 1.9:

Coordinate systems and segment magnet: The coordinate system moving with the target path (blue) forms the basis for all particle coordinates (red: particle path deviating from the target path), which are sensibly specified relative to the target particle. The coordinates of a particle in six-dimensional phase space are therefore $\tilde{y} \tilde{y} \tilde{y} \tilde{y} \tilde{y} \tilde{y}$

$$\tilde{y} \tilde{y} \tilde{y} \tilde{y} \tilde{y} \tilde{y} \tilde{y} \tilde{y} \tilde{y} \tilde{y} \tilde{y} \tilde{y}.$$

With the segment magnet, the entry and exit takes place with the pole edge angle $\tilde{\gamma}$, the deflection angle is $\tilde{\gamma}$ and the bending radius is \tilde{y} .

The black coordinate system is intended for the coordinates of the magnetic field. The $\tilde{y}\tilde{y}$ -axis protrudes into the plane of the drawing or into the interior of the magnet.

The RTM with two $180\tilde{\gamma}$ deflection magnets was already mentioned in 1946 [8]; the flexible arrangement of the deflection magnets allows, for example, the installation of an HF linac and individual focusing elements. In the case of the STM, the entry and exit angles in the deflection magnets are perpendicular to the face of the magnet, so the vertical defocusing effects of the real fringe field are smaller here than with polytrons ($N > 1$) with oblique pole edge angles $\tilde{\gamma}$ [14].

The greatest distance between the nominal orbits of two adjacent orbits in the STM is caused by the transverse dispersion and is $n \cdot \tilde{y}/\tilde{y}$. Thus the distance at an acceleration frequency $\tilde{\gamma} = c/\tilde{y}HF = 2.45$ GHz for $n = 1$ is about 3.9 cm. This distance should always be a few centimeters, for example to be able to install correction magnets on the dispersion tracks [11].

The flight distances in an RTM increase with increasing energy, so that at

1.3 The deflection system and its properties

RTM3 the first circuit is already about 25 m long. This means that angle errors of $\delta\theta \approx 1$ mrad can lead to position errors of $\delta x \approx 25$ mm after just one revolution if no precautions are taken by focusing. Nevertheless, only small local deviations from the target magnetic field can be tolerated: At MAMI, the magnets are corrected by surface correction coils in such a way that for the deviations $|\delta B/B| \approx 10^{-4}$ can be maintained. Then mechanically "small" correction magnets on the dispersion orbits are sufficient to compensate for the remaining deflection errors (typically $|\delta\theta| < 1$ mrad). In addition, this ensures for the longitudinal dynamics that there are no "jumps" in the path length, which in turn would cause non-correctable changes in the target phase ϕ_{target} [11].

1.3.1 Focusing the beam

To minimize the effects of position and angle errors, the beam must be focused. Then a beam deviating from the target path leads to a so-called Betatron vibration around the target path specified by position monitors.

Various methods can be used to focus a beam classified as "weak focus" and "strong focus".

"Weak focusing" has been known since the early days of cyclotrons and betatrons and can be observed with both homogeneous and inhomogeneous deflection magnets (see Figure 1.10). The "weak focusing" of a homogeneous deflection magnet takes place in the deflection plane, there is no focusing effect perpendicular to it. However, a superimposed gradient can also cause weak vertical focus [14]. However, this focusing is very limited and not flexible, since it should deflect and focus horizontally at the same time and also focus vertically, which, however, has fundamental limits (Earnshaw theorem).

Stronger and more flexible focusing can be achieved by alternating gradients ("alternating gradient"), because changing the gradient first focuses in one (eg horizontal) plane and then vice versa. If the distance between the gradient changes is smaller than the individual focal length, then this system has a focusing effect in *both* planes (eg focusing with a quadrupole doublet). Normally, single quadrupole magnets are used in "hard focusing", but solenoid magnets can also be used.

Homogeneous deflection magnets

In a homogeneous magnetic field that is perpendicular to the accelerator plane, there is no vertical focusing. In the horizontal there is a focal point for parallel starting rays ($\delta x = 0$, $\delta\theta = 0$), which is also the reversal point of the ray (see Figure 1.10).

1 The Harmonic Double-Sided Microtron (HDSM)

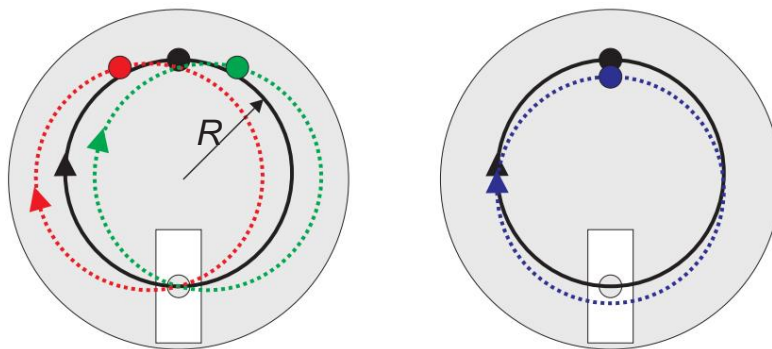


Figure 1.10: Weak focusing

in a homogeneous magnetic field: For magnetic fields $\vec{B} \perp \vec{v}$ perpendicular to the accelerator plane (\vec{v} plane), the target path is a circular path (black). The weak focusing means that the beam always returns to the starting point (red and green) despite angular errors ($\delta\theta$, left) or for spatial errors (δy , right) there are two focal points. There is no focusing in the \vec{v} plane parallel to the magnetic field.

fringing effects

Due to fringe field effects, however, the magnetic field is only homogeneous and parallel to the y -axis inside a magnet; at the pole edges, field components in the z -direction must be expected (Figure 1.9). In principle, this field component leads to a negative vertical focal length f_y [7, 11]:

$$\frac{1}{f_y} = \frac{1}{R^2} \int_{-y/2}^{y/2} dz \left(\frac{dB(z)}{dz} \right) \int_{-y/2}^{y/2} dz \left(\frac{dB(z)}{dz} \right) + \dots \quad (1.8)$$

with the orbit radius R in the homogeneous magnetic field B_0 . The boundary field extends from $y/2$ to 0 in the z -direction. B' here is the derivative dB/dz . However, the defocusing can be compensated for by a suitable choice of the field curve $B(z)$ in the peripheral field area. The opposing field strip according to Babiř and Sedlařek [7, 22] has prevailed as a solution for the RTM: In front of the homogeneous main field B_0 there is an opposing field with B' that is narrow in the z -direction. $y/2 \approx 0.2 B_0$ [23]. In this way, the vertical defocusing can be compensated for in the desired manner.

The B_z components have a much stronger effect if, in the case of the 90° segment magnets, the beam does not enter and exit the magnetic field *perpendicularly*, but rather at an angle. From the point of view of the beam, large B_x components are then present, which further increase the defocusing. Focal lengths of well under 1 m up to a few cm can be expected [6].

1.3 The deflection system and its properties

Field gradient perpendicular to the face of the magnet

Alternatively, instead of homogeneous magnets, a magnet with a gradient along the z -axis can be used to control the vertical defocusing - so-called "combined function" magnets. With increasing energy, the beam penetrates deeper and deeper into the magnet up to the reversal point $z_{\max,i}$ of orbit i . Therefore, for each additional orbit j with $j > i$, the field profile $B(z)$ can be iteratively developed in the range between $z_{\max,i} < z < z_{\max,j}$ without affecting the properties of the previous orbits.

An exponential decay is optimal, since the vertical image then becomes achromatic [23, 24]. With this procedure, the field gradient has been developed – taking into account the production techniques – in such a way that the vertical defocusing is compensated for practically over the entire energy range (Figure 1.11). The average remaining focal length is about 150 m, which can easily be compensated for by the quadrupoles on the linac axes [25].

The result is a magnet with a field gradient whose horizontal and vertical mapping corresponds to a drift path, but whose length is energy-dependent (Figure 1.12) [20, 26].

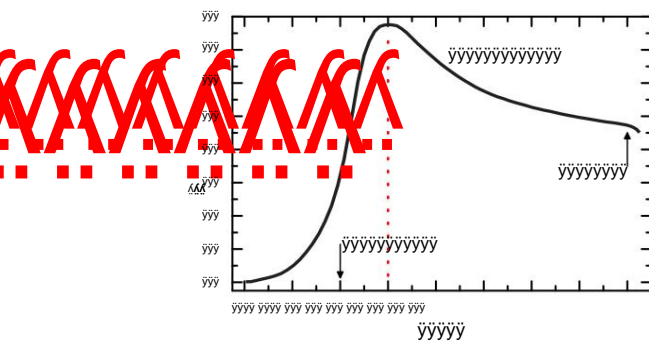


Figure 1.11:
Magnetic field versus distance to the pole edge (y -axis) of an HDSM dipole [27].

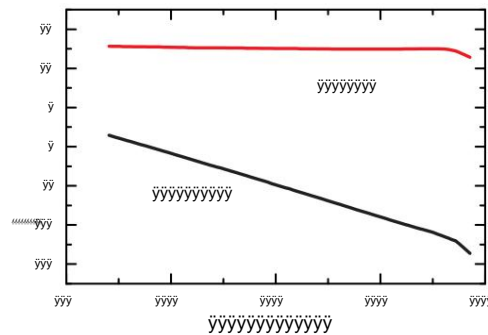


Figure 1.12:
Horizontal and vertical drift distances of a $y\bar{y}$ deflection system [27].

Taking Equation 1.7 into account, this macroscopic field gradient leads to the fact that the constant magnetic field B must be replaced by $\bar{y}B\bar{y} < B$. The reducing effect of the gradient increases from iteration i to iteration j such that $\bar{y}B\bar{y}_j < \bar{y}B\bar{y}_i$ for $j > i$. But Equation 1.7 must be satisfied for all iterations, causing the target energy gain to decrease in the same way. With the right choice of target energy gain and phase, the inherent phase focus automatically leads to a continuous course of the acceleration. Nevertheless, the longitudinal stability needs to be examined more closely (Section 1.4). The field gradient optimized for vertical imaging requires that the energy gain of about 16.8 MeV at the shot energy

1 The Harmonic Double-Sided Microtron (HDSM)

around 14 MeV at reject energy decreases; still around 17%, which is shown in Figure 1.13 [26].

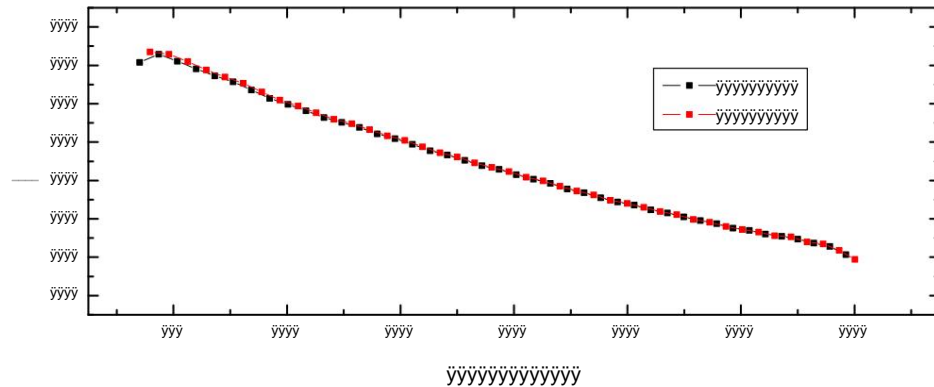


Figure 1.13:

Desired energy gain in HDSM: The field gradient requires the energy gain to decrease from around 17% over the course of acceleration.

Advantages of the telecentric segment magnet

Telecentricity enables the deflection system to be handled comparatively easily during operation, because essentially only drift paths need to be taken into account.

Because the deflection magnets have the desired telecentric properties, focusing is ideally done exclusively by quadrupoles on the linac axes⁷, as is the case with the STMs on MAMI. Various other focusing schemes are also discussed in detail in [26] and rejected compared to this simple scheme because they have no fundamental advantages over the method outlined.

1.3.2 Longitudinal Focusing

The combination of recirculation with longitudinal dispersion and a linac has a longitudinal focusing effect, since relativistic electrons ($v \approx c$) with an energy deviation $\delta E > 0$ fly a slightly longer path through the longitudinal dispersion compared to the target particle and thus arrive at the HF resonator somewhat later. If the phase of the high-frequency is chosen so that the target particle lies on the falling edge, the electron with $\delta E > 0$ is accelerated somewhat less strongly by the HF and approaches the target particle in the next orbit, i.e. it follows a so-called synchrotron oscillation

⁷The focal length of a quadrupole magnet increases with δE , while that of a doublet increases with δE^2 , so that doublet focusing decreases drastically with increasing energy. This effect is unproblematic because the energy is only roughly doubled with the HDSM.

1.4 Periodic Systems: Fundamentals of Longitudinal Dynamics

around the target phase $\bar{\psi}$. Figure 1.2 already shows the effect of phase focusing; the theoretical background is explained in Section 1.4.

Choice of target phase $\bar{\psi}$

An electromagnetic wave (or the electric field) is:

$$\begin{aligned} E_y(\bar{y}x, t) &= E_0 e^{i(\bar{y} k \bar{y}x - \bar{y} H t)} \\ &= E_0 e^{i\bar{y}} \end{aligned} \quad (1.9)$$

Since a standing wave forms in the (stationary) resonator, $\partial A / \partial x = 0$ and thus $\bar{y} = \bar{y} H t$. Therefore, in this notation, the phase \bar{y} for a particle with $\bar{y} E > 0$ is *smaller* (or more negative) than that of the target particle due to longitudinal dispersion. The target energy gain $\bar{y} E_{\text{Soll}}$ of a single resonator or a linac is:

$$\bar{y} E_{\text{Soll}} = e U_0 \cos(\bar{y}_{\text{Soll}}) \quad (1.10)$$

with $\bar{y}_{\text{set}} < 0$ in this convention. The target phase of the RTMs is therefore always negative.

1.4 Periodic Systems: Fundamentals of Longitudinal Dynamics

In a periodic system, it must be avoided that minor incorrect settings lead to deviations increasing beyond all limits (e.g. an energy gain $\bar{y} E = \bar{y} E_{\text{Soll}}$ causes phase deviations $\bar{y} \bar{y}_i = \bar{y}_{\text{Soll}} \bar{y}_i$ in a later cycle i).

The basics of longitudinal dynamics can be found in great detail in various works (e.g. [7, 14]) and are therefore only summarized here.

1.4.1 Description by the linear beam dynamics

With the means of linear jet dynamics, simple conditions can be formulated to check the stability, under which a periodically stable acceleration can take place. This will be shown later using the example of the longitudinal phase space $(\bar{y}, \bar{y} E)$.

The derivation of the matrix formalism used for this from the Hamilton-Lagrange formalism and the vector potentials of the various accelerator components can be found in numerous publications [14]. Here follows a short summary of the original derivation [20].

1 The Harmonic Double-Sided Microtron (HDSM)

1.4.2 Matrix formalism of jet dynamics

The motion of a single electron in external electromagnetic fields is described by the Hamiltonian $H(\tilde{y}v)$ with $\tilde{y}v = (\tilde{y}x, \tilde{y}p_x, \tilde{y}y, \tilde{y}p_y, \tilde{y}, \tilde{y}E, \tilde{y}z)$, where $\tilde{y}x, \tilde{y}y, \tilde{y}p_x, \tilde{y}p_y$ are the coordinates or the impulses related to the target particle and further \tilde{y} and $\tilde{y}E$ determine the phase and energy deviation.

The coordinate z corresponds to the distance covered along the target path and is "fixed" for highly relativistic particles with the phase \tilde{y} or the deviations $\tilde{y}\tilde{y}$.

With a matrix S

$$S = \begin{pmatrix} \tilde{y} & 0 & 1 & 0 & 0 & 0 & \tilde{y} \\ 0 & 1 & 0 & 0 & 0 & 0 & \\ 0 & 0 & 0 & 1 & 0 & 0 & \\ 0 & 0 & \tilde{y} & 1 & 0 & 0 & \\ 0 & 0 & 0 & 0 & 0 & 1 & \\ 0 & 0 & 0 & 0 & \tilde{y} & 1 & 0 \end{pmatrix} \quad (1.11)$$

the movement of a particle is calculated from the Hamilton function:

$$\frac{d\tilde{y}v}{dz} = \frac{\partial H}{\partial \tilde{y}v} S \quad (1.12)$$

If only the Jacobian matrix J of $H(\tilde{y}v)$ is taken into account, a solution is possible by integration over the distance z :

$$\tilde{y}v(z) = \tilde{y}v(0) + \int_0^z J(s) \tilde{y}v(s) ds \quad (1.13)$$

For a J that is independent of z (ie for a drift path, for a movement in a homogeneous magnetic field, etc.), the following applies in particular

$$\tilde{y}v(z) = e^{Jz} \tilde{y}v(0) = M(z) \tilde{y}v(0) \quad (1.14)$$

where $M(z)$ in the linear beam optics then the above mentioned section of the accelerator describes.

For a real beam guidance consisting of n individual such sections, which here are denoted by $i \in [1, n]$, the solution for $\tilde{y}v(z)$ is therefore given:

$$\tilde{y}v(z) = M_n M_{n-1} \dots M_2 M_1 \tilde{y}v(0) \quad (1.15)$$

In the case of the longitudinal phase space, $\tilde{y}v(0) = (\tilde{y}y_{\text{before}}, \tilde{y}E_{\text{before}})^T$ and analogously $\tilde{y}v(z) = (\tilde{y}y_{\text{after}}, \tilde{y}E_{\text{after}})^T$. The transformation matrix M is the product of the matrices M_i . Equation 1.15 can then be written as follows:

$$\tilde{y}v_{\text{after}} = M \cdot \tilde{y}v_{\text{before}} \quad (1.16)$$

1.4 Periodic Systems: Fundamentals of Longitudinal Dynamics

In a recirculating accelerator, a sequence of accelerator components is flown through several times. The smallest repetitive sequence is called the *unit cell*, which can be used to characterize the longitudinal dynamics of a microtron.

The development of the longitudinal phase space consisting of phase and energy deviations \ddot{y} and $\ddot{y}E$ is essentially determined by the magnetic field of the deflection magnets and by the acceleration distances. Equation 1.17 thus describes the transformation of a circuit i consisting of a linac Li and a deflection system Di :

$$\ddot{y}_{\text{after}} \ddot{y} = Di Li \ddot{y}_{\text{before}} \ddot{y}E_{\text{before}} \ddot{y} \quad (1.17)$$

In the explanations that now follow, the circulation index i is omitted since i has no special function here. In the case of the DSM, however, the corresponding matrices also change as a result of the desired phase shift.

dipole matrix

The matrix D of the dipole acts as an energy-dependent drift path: the energy is not changed, only the phase deviation is subject to an energy-dependent transformation. For this purpose, the length of the drift with the matrix element D_{12} is selected in such a way that an "energy offset" $\ddot{y}E$ corresponding to the target energy gain $\ddot{y}ESoll = eU_0 \cos(\ddot{y}soll)$ leads to a phase change of $n 360^\circ$ or $n 2\pi$ in order to fulfill the coherence condition:

$$D = \ddot{y} \begin{pmatrix} 1 & \ddot{y}^0 \\ \frac{n 2\pi}{eU_0 \cos(\ddot{y}set)} & 1 \end{pmatrix} \ddot{y} \quad (1.18)$$

The sign of D_{12} takes into account the choice of the desired phase ($\ddot{y}Soll < 0$) defined in Section 1.3.2, since $\ddot{y}E < 0$ means a shorter transit time and the electron must therefore experience an acceleration greater than $\ddot{y}ESoll$.

linac matrix

The matrix L of the linac, on the other hand, should not change the phase deviation \ddot{y} because the electrons are relativistic and the linac is designed for $v = c$. However, a phase deviation \ddot{y} leads to a different energy gain:

$$\ddot{y}E = \ddot{y}ESoll + \ddot{y}Enach = eU_0 \cos(\ddot{y}soll + \ddot{y}) \quad (1.19)$$

In this notation, a linac behaves in a fundamentally non-linear manner, because in this expression the phase deviation \ddot{y} appears as an argument of the cosine function. To the behavior

1 The Harmonic Double-Sided Microtron (HDSM)

To be able to easily investigate the longitudinal dynamics, a linearization makes sense:

$$\begin{aligned} \ddot{y} E_{\text{nach}} &= \ddot{y} E - \ddot{y} E_{\text{set}} = \\ &= eU_0 \cos(\ddot{y}_{\text{set}} + \ddot{y}) - eU_0 \cos(\ddot{y}_{\text{set}}) \\ &\approx -\ddot{y} eU_0 \sin(\ddot{y}_{\text{set}}) \end{aligned} \quad (1.20)$$

Here the expression in the last line of Equation 1.20 was approximated by the time derivation of the field profile, which is continued with the matrix element L21 :

$$L = \ddot{y} eU_0 \sin(\ddot{y}_{\text{setpoint}}) \quad (1.21)$$

The effect of L corresponds to focusing.

Acceleration approximated as a linear mapping

Because both matrices do not change at all (RTM, homogeneous magnetic field) or only slightly (DSM, field gradient) from one revolution to the next, one revolution can be viewed as an elementary cell of the periodic acceleration process. The entire acceleration process from cycle 1 to n is then described by the matrix product :

$$\ddot{y} \ddot{y} E_n = D_n L_n D_n \ddot{y} \ddot{y} E_1 \quad \dots \quad D_2 L_2 D_1 L_1 \ddot{y} \ddot{y} E_1 \quad (1.22)$$

1.4.3 Stability, intrinsic ellipse and resonance phenomena

Stability in the sense mentioned requires that the transformation matrix M of the unit cell corresponds to a special similarity mapping (or a rotational stretching) with eigenvalues $|\ddot{y}| = e^{\pm i\ddot{y}}$ and corresponds to the angle of rotation \ddot{y} . Since, according to Liouville's theorem, the volume of phase space under the action of conservative forces⁸ is a conserved quantity, the following applies:

$$\det(M) \approx 1 \quad (1.23)$$

If both conditions are fulfilled, the repeated application of the transformation matrix M does not lead to an unlimited increase in the input *deviations* $\ddot{y} \ddot{y} 0$ and $\ddot{y} E 0$, but the deviations describe points on the so-called eigenellipse from revolution to revolution, which is called synchrotron oscillation (longitudinal) or betatron oscillation (transverse). It is to be observed. The angle \ddot{y} by which the points move on from revolution to revolution on this ellipse is the so-called longitudinal

⁸The static magnetic fields of the deflection magnets and the electric fields of the acceleration sections can be represented as a gradient of a potential [28].

1.4 Periodic Systems: Fundamentals of Longitudinal Dynamics

Phase advance \tilde{y} , which is often expressed as the operating point ("tune") $q = \tilde{y}/2\tilde{y}$. Then the matrix U corresponds to the original matrix M :

$$U = \begin{pmatrix} \tilde{y} \cos(\tilde{y}) & \tilde{y} \sin(\tilde{y}) \\ -\tilde{y} \sin(\tilde{y}) & \tilde{y} \cos(\tilde{y}) \end{pmatrix} \tilde{y} \tilde{y} M \quad (1.24)$$

The Twiss parameters \tilde{y} , \tilde{y} and \tilde{y} are subject to the condition $\tilde{y} \tilde{y} \tilde{y}^2 = 1$ and can be determined from M by comparing the matrix elements. The Twiss parameters determine the area (acceptance), eccentricity and orientation (convergent/divergent) of the eigenellipse.

At the same time applies

$$\text{Trace}(U) = 2 \cos(\tilde{y}), \quad (1.25)$$

ie one can calculate the phase shift \tilde{y} directly from the matrix M and recognize under which conditions the transformation is periodic and not resonant:

$$|\text{Trace}(M)| \leq 2 \quad (1.26)$$

For an RTM this means:

$$\text{Trace}(M_{RTM}) = \text{Trace}(L D) = 1 \tilde{y} \quad (1.27)$$

$$eU0 \sin(\tilde{y}) + 1 eU0 \cos(\tilde{y}) = 2 + n \tilde{y} \tan(\tilde{y})$$

The target phase $\tilde{y}_{\text{target}}$ can be determined from the phase advance \tilde{y} :

$$\tilde{y}_{\text{setpoint}} = \arctan \frac{1}{\tilde{y} \cos(\tilde{y})} \quad (1.28)$$

With $|2 + n \tilde{y} \tan(\tilde{y})| \leq 2$, a periodic acceleration follows for $\tilde{y} \in [0, 32.5^\circ]$ in the case of an RTM with harmonic number $n = 1$. With a DSM, the matrix D_i must be taken into account that the total energy gain of a complete circuit (with two linacs $\tilde{y}E$) must produce a path length increase of 360° per deflection system due to longitudinal dispersion. Therefore, in the previous derivation of the RTM, the expression $\tilde{y}E = eU0 \cos(\tilde{y}_{\text{soll}})$ should be replaced by $2\tilde{y}E$ for the DSM:

$$\text{Spur}(M_{DSM}) = \text{Spur}(L D) = 1 \tilde{y} \quad (1.29)$$

$$eU0 \sin(\tilde{y}) + 1 eU0 \cos(\tilde{y}) = 2 + n \tilde{y} \tan(\tilde{y})$$

A stable periodic acceleration is therefore possible for $\tilde{y} \in [0, 51.85^\circ]$ at $n = 1$ [6, 29]. This comparatively large stability range is at least partially required by the field gradient of the deflection magnets.

Figure 1.14 shows the transformation of the phase space in two examples different phase advances \tilde{y} .

1 The Harmonic Double-Sided Microtron (HDSM)

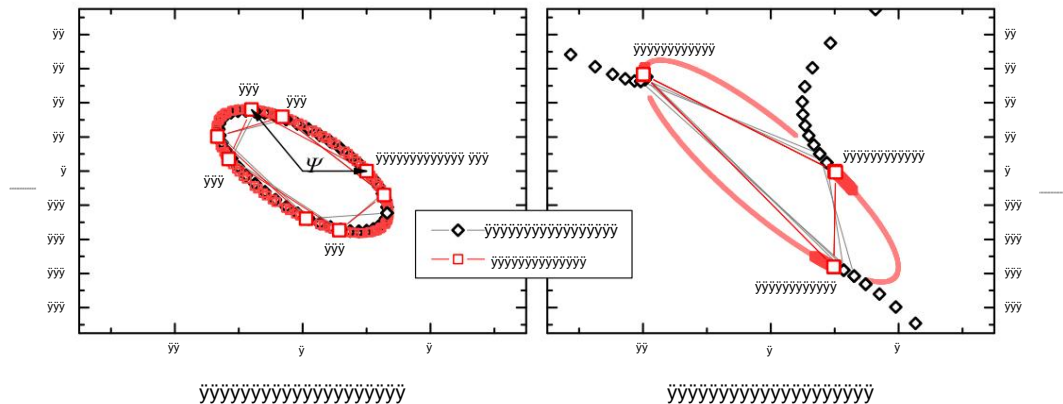


Figure 1.14:

Eigenellipse and resonance (RTM3): Transformation of a phase space from the starting point $(+1\bar{y}, 0 \text{ keV})$ for 100 periods, the first eight are connected by lines. The eigenellipse is shown on the left with a phase advance \bar{y} of about $84.3\bar{y}$ ($\bar{y} \bar{y} \bar{y} \bar{y} \bar{y} \bar{y} \bar{y} \bar{y}$). The differences between the complete calculation and the linearization are hardly noticeable. On the right, the eigenellipse is already very degenerate near $\bar{y} \bar{y} 120\bar{y}$ ($\bar{y} \bar{y} \bar{y}$ resonance). Here you can also see that only the full calculation shows the resonance peak (black diamonds); the linearization remains limited even after many orbits and eventually sweeps the entire edge, represented by the faint red curve.

"Adaptation" (matching) of the injected phase space

So far (and especially in Figure 1.14) only a punctiform ray has been considered, which describes the center of gravity of a real and extended bunch.

The distribution in the bunch extends over an area in phase space whose size is determined by the emittance⁹ of the beam. In order to distort the phase space as little as possible due to non-linearities (see above), the orientation of the injected phase space distribution should correspond to the system's own ellipse, otherwise the particles from the edge areas of the injected phase space will unnecessarily reach larger oscillation amplitudes. However, if the injected phase space is directed into the center of acceptance with the correct orientation, this is referred to as an "adapted" beam.

In order to achieve this, a suitable beam guidance is required in the transverse phase space, which rotates the phase space into the required orientation (eg divergent beam, parallel beam, etc.) with the help of quadrupole magnets and drift paths.

For the longitudinal phase space from $\bar{y}\bar{y}$ and $\bar{y}E$ this means that by a combination of acceleration and deflection system the orientation of the phase space

⁹The emittance describes the size of the spatial and momentum distribution.

can be adjusted to the proper ellipse. In the case of the HDSM, this adjustment in the injection beam guidance begins with the so-called “matching section” (MS, a short acceleration section, Figure 1.6), which the beam is intended to traverse in the vicinity of the zero crossing of the electric field. This does not change the mean energy of the beam, but the focusing effect of the gradient can be exploited to optimize the phase space upon arrival at the 4.9 GHz linac. Because that alone is not enough, the 4.9 GHz linac is injected during a *positive* phase. A small magnetic chicane extends the path length between the 4.9 GHz linac and the 2.45 GHz linac by about 10γ or 4.9 GHz, so that after this chicane the acceleration continues at phases $\gamma < 0\gamma$ [20, 26]. Apart from that, the matching section is used later in the measurements to vary the injection energy by around ± 1 MeV.

Synchrotron oscillation and optimization of longitudinal optics

A deviation ($\gamma\gamma$, γE) of the beam from the target particle leads to the beam describing an ellipse with the phase advance γ around the target particle. If several orbits i are considered, the phase deviations $\gamma\gamma i$ (as a projection of this ellipse onto the phase coordinates) can be measured that a synchrotron oscillation

$$\gamma\gamma i = AS \sin(\gamma i + \gamma_0) \quad (1.30)$$

describe. Both are shown in Figure 1.15. AS is the amplitude of the phase variations $\gamma\gamma i$ and γ_0 the phase of the synchrotron oscillation when it first reaches the linac, which is linked to the phase of the particle on its own ellipse via the Twiss parameters [20].

Due to the more strongly varying injection *phases* $\gamma_{4.9}$ and $\gamma_{2.45}$ compared to the RTM, the Twiss parameters are also subject to larger fluctuations. Nevertheless, if the amplitude AS and phase γ_0 are known, the approximate deviation ($\gamma\gamma_0$, γE_0) can be calculated and corrected if necessary. This is verified empirically in Section 4.5 and has since been used to optimize the HDSM.

resonances

If γ is too close to a rational quotient of 2π (e.g. $\gamma = \pi$, $\gamma = \pi/2$, $\gamma = \pi/3$...), resonance phenomena can be observed that further amplify existing errors (see Figure 1.14). The matrix calculations can determine the phase shift γ well, but the resonance peaks cannot be made visible with this method.

1 The Harmonic Double-Sided Microtron (HDSM)

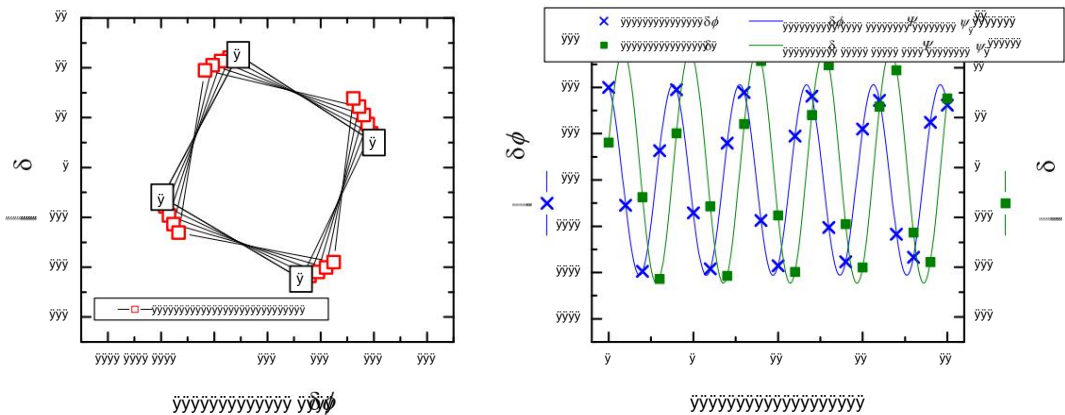


Figure 1.15:

Eigenellipse and synchrotron oscillation (injection HDSM 4.9 GHz: 9 MV, \ddot{y} ; 2.45 GHz: 9 MV, $\ddot{y}\ddot{y}$, linearized method): Analogous to Figure 1.14, the eigenellipse of the starting point (+1 \ddot{y} , 10th keV) for 20 “recirculations”, which is close to the \ddot{y} resonance ellipse is shown as a synchrotron oscillation, to which a function $\ddot{y} \ddot{y} \ddot{y}\ddot{y}\ddot{y} \ddot{y} \ddot{y}\ddot{y}$ was fitted for $\ddot{y}\ddot{y}$ and $\ddot{y}\ddot{y}$. The measurable phase deviations \ddot{y} are used in Section 4.5 to correct the injected beam with the help of amplitude $\ddot{y} \ddot{y} \ddot{y}$ and initial phase \ddot{y} of the phase curve.

1.4.4 Influence of the magnetic field gradient on the longitudinal dynamics

In the coherence condition according to Equation 1.7, the gradient of the magnetic field leads to a smaller average magnetic field $\ddot{y}\ddot{y}$ that the beam experiences in a given revolution i . This in turn leads to a correspondingly smaller energy gain $\ddot{y}Ei$, which, however, occurs automatically in the microtron due to the phase focusing, in that the target phase $\ddot{y}\ddot{y}_{\text{Soll},i}$ matching the correct energy gain is met. Therefore it will run through a certain interval $\ddot{y} \ddot{y} [\ddot{y}0, \ddot{y}1]$ from injection to extraction.

With the ideally symmetrical DSM, both linacs are operated with the same HF amplitude $U0$, and the bullet phase \ddot{y} is also identical for both linacs.

Deviations from symmetry due to errors (e.g. HF amplitude, bullet phase, adjustment) mean that the bullet phases $\ddot{y} \ddot{y} \ddot{y}1, \ddot{y}2$ in both linacs can exhibit an offset $\ddot{y} \ddot{y} = 0\ddot{y}$:

$$\ddot{y} = \ddot{y}2 \ddot{y} \ddot{y}1 \quad (1.31)$$

For small \ddot{y} , a mean and fictitious phase $\ddot{y}\ddot{y}$ can be defined in order to fulfill the coherence condition with the resulting mean energy gain of both linacs [26]:

$$\cos(\ddot{y}1) + \cos(\ddot{y}2) = 2 \cos(\ddot{y}\ddot{y}) \quad (1.32)$$

Because of the definition of \ddot{y} , the easiest way to change its magnitude is to change the

1.5 The Harmonic Double-Ended Microtron as a Special Case for MAMI-C

Bullet phase $\tilde{\gamma}_2$ in the second linac must be controlled, which must be considered more closely in the HDSM (especially in Chapter 4, Section 4.5.4).

1.4.5 Longitudinal stability of the DSM

In order to investigate the stability, different target phases $\tilde{\gamma}_1$ and $\tilde{\gamma}_2$ must be assumed in both linacs of the DSM. This means that the unit cell is no longer a half circuit, but must consider both linacs separately through M1 and M2 :

$$\begin{aligned} \text{Trace}(M) &= \text{Trace}(L_2 D L_1 D) n \tilde{\gamma} \\ &= \tilde{\gamma}^2 + \frac{\sin(\tilde{\gamma}_2)}{\cos(\tilde{\gamma}_1)} \tilde{\gamma}^2 + \frac{n \tilde{\gamma} \sin(\tilde{\gamma}_1)}{\cos(\tilde{\gamma}_1)} \tilde{\gamma}^2 \end{aligned} \quad (1.33)$$

The result is no longer an interval of stable acceleration, but a two-dimensional surface over the phase coordinates $\tilde{\gamma}_1$ and $\tilde{\gamma}_2$ of the two linacs.

However, it is tacitly assumed here that $U_{0.1} = U_{0.2}$ applies to the RF amplitudes of Linac 1 and 2.

The trace of Equation 1.33 is shown in Figure 1.16. There it becomes clear that deviations from symmetry ($\tilde{\gamma}_1, i \neq \tilde{\gamma}_2, i$) lead to the stable region near $\tilde{\gamma}_{32.5}$ being interrupted by a stop band, ie the stability diagram breaks up into two disjoint subregions. Apart from that, some longitudinal resonances have to be traversed, but this is unproblematic due to the small number of orbits in the critical area.

Stop band at $\tilde{\gamma}_{32.5}$ is problematic

For stable operation of the accelerator, it is therefore essential to ensure that that the unstable region around the $\tilde{\gamma}_{32.5}$ resonance can be avoided, resulting in the following section is shown.

1.5 The harmonic double-sided microtron as a special case for MAMI-C

After the field profile $B(z)$ optimized for transversal imaging properties requires a change in the target phase $\tilde{\gamma}_{\text{Soll},i}$ from one revolution i to the next, serious difficulties in the longitudinal dynamics $/2$ resonance in the last revolutions were to be expected when operating with two $\tilde{\gamma}_{32.5}$ is reached, which is due to the strong focusing effect of the $\tilde{\gamma}_{32.5}$ resonance for $\tilde{\gamma}_{32.5}$.

However, if one considers the phase $\tilde{\gamma}$ as a time coordinate, one finds that this matrix element is also affected by the frequency, because the energy deviation

1 The Harmonic Double-Sided Microtron (HDSM)

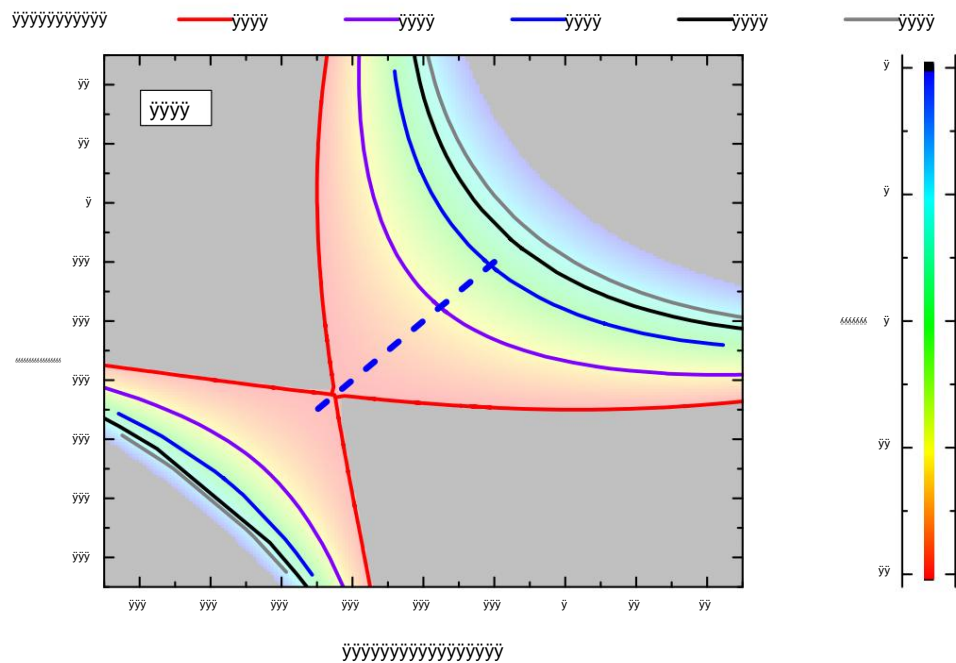


Figure 1.16:

Longitudinal stability area of the DSM: The colored area represents the longitudinal area more stable acceleration (representation a little fainter to avoid the resonance lines and the phase curve to be emphasized). The colors represent the trace of the unit cell matrix (grey $\ddot{y}\ddot{y}$ unstable). Resonances that occur are represented by the solid colored lines.

The blue dotted line represents the planned phase progression [26]. In the DSM at a Bullet phase of $\ddot{y}\ddot{y}\ddot{y}$ which $\ddot{y}\ddot{y}\ddot{y}$ -, $\ddot{y}\ddot{y}$ - and even the $\ddot{y}\ddot{y}$ resonance crossed. The stability area has practically no extension at $\ddot{y}\ddot{y}32.5\ddot{y}$. As a result, even small phase errors in this Area to instabilities, which in turn can easily lead to beam losses.

\ddot{y} After passing the linac (see equation 1.20) depends on the phase $\ddot{y} = \ddot{y}t$ and thus also from the frequency \ddot{y} (w/o \ddot{y} Evor \ddot{y} 0):

$$\begin{aligned}
 \ddot{y}Enach &= eU0 \cos(\ddot{y} + \ddot{y}\ddot{y}) \ddot{y} eU0 \cos(\ddot{y}) \\
 &= eU0 \cos(\ddot{y}(t + \ddot{y}t)) \ddot{y} eU0 \cos(\ddot{y}t) \\
 &\stackrel{\text{is}}{=} \int_0^t eU0 \cos(\ddot{y}t) \ddot{y}t \\
 &= \ddot{y}\ddot{y}eU0 \sin(\ddot{y}t) \ddot{y}t
 \end{aligned}
 \tag{1.34}$$

This corresponds to the fact that a linac with a higher frequency is replaced by a comparatively larger one matrix element L21 is written; lower frequencies reduce the matrix element correspondingly (especially if the target phase is the same, $L21,2^{1.45} = /2L21,4.9$). In Figure 1.17 the two different frequencies (4.9 GHz and 2.45 GHz) are shown.

1.5 The Harmonic Double-Ended Microtron as a Special Case for MAMI-C

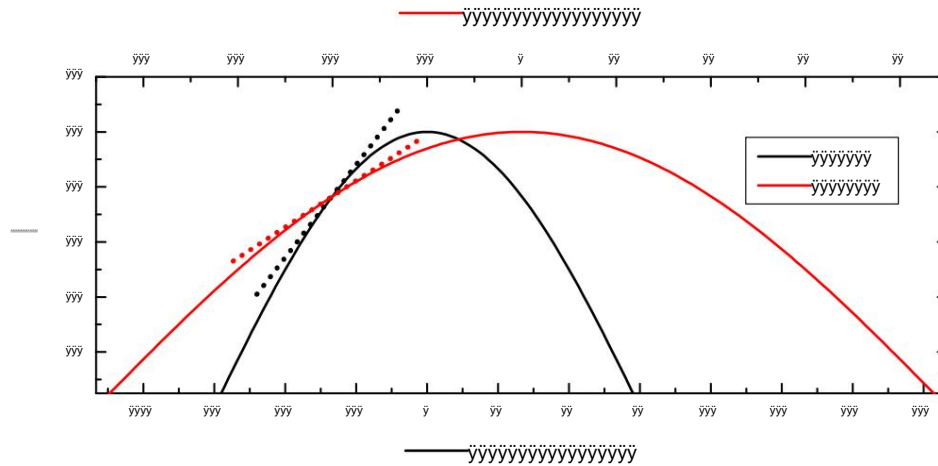


Figure 1.17:

Linac matrix element at two frequencies: The subharmonic frequency (red, 2.45 GHz) causes with the same target phase (here: $\bar{\gamma} \bar{\gamma} \bar{\gamma} \bar{\gamma}$) due to the flatter gradient (see equation 1.34). Halving the focusing power $\bar{\gamma} \bar{\gamma}$ compared to 4.9 GHz, which is shown by the dotted lines

becomes.

In the further course, phase information usually refers to the fundamental frequency of the corresponding linac (e.g. $\bar{\gamma} 2.45 = \bar{\gamma} 32.5 \bar{\gamma}$). In the case of $\bar{\gamma}$, where both frequencies meet, the information will be on the basic frequency of the HDSM - i.e. on 4.9 GHz - referenced.

1.5.1 Subharmonic margin

Now it is already noticeable in Figure 1.8 that the omission of every second bunch leads to the fact that in one of the two linacs also only every second accelerating resonator is occupied by electrons. Exactly this situation applies to MAMI-C: The beam is shot into the 4.9 GHz system of the DSM with a refresh rate of 2.45 GHz. Therefore, one of the two linacs can be operated at 2.45 GHz, which is the longitudinal. Significantly improved stability as intended.

Course of the target phase in the HDSM

The target phase changes of the two HDSM linacs from circuit to circuit are completely determined by the field gradient, since the coherence condition (equation 1.5) is met. Only the entry phases $\bar{\gamma} 4.9$ and $\bar{\gamma} 2.45$ are arbitrary at first, but that Stability criterion according to Equation 1.26 should be fulfilled for all circuits. Besides that

1 The Harmonic Double-Sided Microtron (HDSM)

should the $\frac{1}{2}$ resonance can be avoided with a sufficient safety margin¹⁰.

This problem is dealt with in detail in [26]. In summary, it should be noted here that the ideal phase curve in the 4.9 GHz linac is between 0° and 32.5° (corresponding to the stable range of an STM); the phase curve in the 2.45 GHz linac should then be between 32.5° and a maximum of 51.85° .

1.5.2 Longitudinal stability of the HDSM

The symmetry of both linacs of the DSM is no longer present with the HDSM. Therefore, the elementary cell of the HDSM is the product of {180° deflection, 4.9 GHz linac, 180° deflection, 2.45 GHz linac} - i.e. a complete revolution -. The target energy gain γE must be divided between both linacs:

$$\gamma E = \gamma E_{4.9} + \gamma E_{2.45} \quad (1.35)$$

$$\gamma E_{4.9} = eU_{4.9} \cos(\gamma_{4.9}) \quad (1.36)$$

$$\gamma E_{2.45} = eU_{2.45} \cos(\gamma_{2.45}) \quad (1.37)$$

In Equation 1.21, the target energy gain of the respective linac must therefore be used in the expression for L_i and the total energy gain in D_i . Accordingly, the trace of the longitudinal circulation matrix reads:

$$\gamma E \frac{2\gamma E_{2.45}}{\gamma E} \tan(\gamma_{2.45}) \gamma \gamma E_{4.9} 2 + \frac{2\gamma}{\gamma E} \frac{2\gamma \gamma 1 + \frac{\gamma E_{2.45}}{\gamma E} \tan(\gamma_{2.45}) \gamma \gamma}{\gamma E} \tan(\gamma_{4.9}) \quad (1.38)$$

Figure 1.18 shows the resulting stability area of the HDSM.

1.5.3 Consequence of target phase change in HDSM

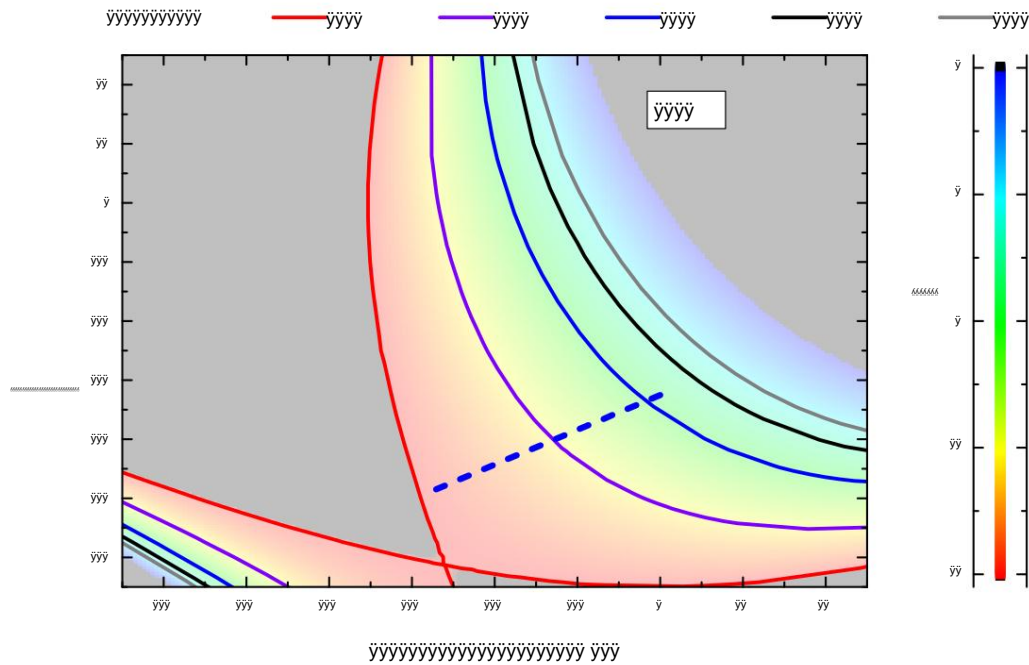
The energy gain $\gamma E = \gamma E_{4.9} + \gamma E_{2.45}$ causes a change in flight time from round to round, which is why the arrival time of the jet in both linacs changes by a similar amount. However, this change in flight time means that at different frequencies, for example, a 1° phase change at 4.9 GHz corresponds to only 0.5° at 2.45 GHz and the target phase change runs differently. Therefore Equation 1.31 has to be modified:

$$\gamma = 2\gamma_{2.45} \gamma \gamma_{4.9} \quad (1.39)$$

γ is determined by the selection of the two entry phases $\gamma_{4.9}$ and $\gamma_{2.45}$; So if you want to change γ , for example, but leave the insertion phase in the 4.9 GHz linac, you can use the insertion phase in the 2.45 GHz linac to specify γ .

¹⁰The bunch length at MAMI is typically 2γ related to 2.45 GHz [30, 31]. The safety distance should correspond to this extension.

1.5 The Harmonic Double-Ended Microtron as a Special Case for MAMI-C

**Figure 1.18:**

Longitudinal stability area of the HDSM: Representation as in Figure 1.16. The phases $\tilde{\gamma}\tilde{\gamma}\tilde{\gamma}\tilde{\gamma}$ and $\tilde{\gamma}\tilde{\gamma}\tilde{\gamma}\tilde{\gamma}$ of the two linacs refer to the respective frequency. The blue dotted line represents the planned phase progression [26]. The bullet phases in HDSM are $0\tilde{\gamma}$ (4.9 GHz) and $\tilde{\gamma}\tilde{\gamma}\tilde{\gamma}\tilde{\gamma}\tilde{\gamma}$ (2.45 GHz) and only the $\tilde{\gamma}\tilde{\gamma}$ and $\tilde{\gamma}\tilde{\gamma}$ resonances must to be crossed. Investigations on this in Chapter 4.

Impact on the distribution of energy gain to both linacs

Ideally, the energy gain of one orbit should be distributed equally to both *linacs* distribute – as with the DSM:

$$\tilde{\gamma}Ei = eU_{4.9} \cos(\tilde{\gamma}4.9,i) + eU_{2.45} \cos(\tilde{\gamma}2.45,i) \quad (1.40)$$

With

$$eU_{4.9} \cos(\tilde{\gamma}4.9,i) \tilde{\gamma} eU_{2.45} \cos(\tilde{\gamma}2.45,i) \tilde{\gamma} \frac{1}{2}\tilde{\gamma}E_{gg} \quad (1.41)$$

With a constant target *phase* $\tilde{\gamma}i$, this is not a problem, but due to the target phase change the ratio ri of the two energy *gains* $\tilde{\gamma}E_{4.9,i}$ and $\tilde{\gamma}E_{2.45,i}$ will change.

That makes:

$$ri := \frac{\tilde{\gamma}E_{4.9,i}}{\tilde{\gamma}E_{2.45,i}} = \frac{eu_{4.9}}{eu_{2.45}} \cdot \frac{\cos(\tilde{\gamma}4.9,i)}{\cos(\tilde{\gamma}2.45,i)} \quad (1.42)$$

1 The Harmonic Double-Sided Microtron (HDSM)

Since the ratio of the amplitudes $U_{4.9}/U_{2.45}$ is constant, only the second fraction with the cosine functions has to be considered. Substituted with Equation 1.39, the newly defined r_{yi} is:

$$r_{yi} := \frac{\cos(\tilde{y}_i)}{\cos((\tilde{y}_i + \tilde{y})/2)} \quad (1.43)$$

However, this ratio of the two energy gains is *not* constant during acceleration due to the change in the target *phase* \tilde{y}_i . Nevertheless, it should vary as little as possible in order to distribute the energy gain evenly over both linacs for all circuits. The choice of the entry *phases* $\tilde{y}_{4.9}$ and $\tilde{y}_{2.45}$ (and thus also of \tilde{y}) should take this into account.

A favorable situation arises, for example, with identical amplitudes when the phase in the 4.9 GHz linac wanders from $0\tilde{y}$ to $30\tilde{y}$ and simultaneously in the 2.45 GHz from $20\tilde{y}$ to $35\tilde{y}$ ($\tilde{y} = 40\tilde{y}$), since in this case the quotient $r_{yi} = \cos(\tilde{y}_i)/\cos((\tilde{y}_i + \tilde{y})/2)$ remains relatively constant in the corresponding phase interval (Figure 1.19, green curve). However, a value for $\tilde{y} = 70\tilde{y}$ (injection *phases* $\tilde{y}_{4.9} = 0\tilde{y}$ and $\tilde{y}_{2.45} = 35\tilde{y}$) was planned, on the one hand to avoid the $1/2$ resonance and on the other hand to ~~the energy gain for a given rotation is field gradient provided~~ by the 4.9 GHz linac (r_{yi} runs from approx. 1.2 to 1.35).

This simplified consideration (here with identical amplitudes) is only intended to clarify that the distribution of the energy gain between the two linacs can be decisively influenced solely by the selection of the injection *phases* $\tilde{y}_{4.9}$ and $\tilde{y}_{2.45}$. Chapter 4 explores this further.

Figure 1.20 shows the influence of different HF amplitudes on the trace of the longitudinal matrix.

1.5.4 Consequences in operation and for jet dynamic investigations

The previous sections have made it clear that a double-sided microtron is well suited as a post-accelerator for MAMI. The field gradient of the deflection magnets greatly simplifies the vertical optics – on the other hand, it forces a non-negligible change in the target phase during acceleration. The harmonic double-ended microtron cleverly bypasses the critical longitudinal

$1/2$ resonance - first on paper.

The challenge now is to set this planned configuration on the real machine, examine it, optimize it and classify it using the stability diagram in Figure 1.18, for example.

Therefore, methods must be developed to record the relevant parameters as precisely as possible. The HF amplitudes $U_{4.9}$ and $U_{2.45}$ and the associated phases $\tilde{y}_{4.9,i}$ and $\tilde{y}_{2.45,i}$ of the individual revolutions i are particularly important.

1.5 The Harmonic Double-Ended Microtron as a Special Case for MAMI-C

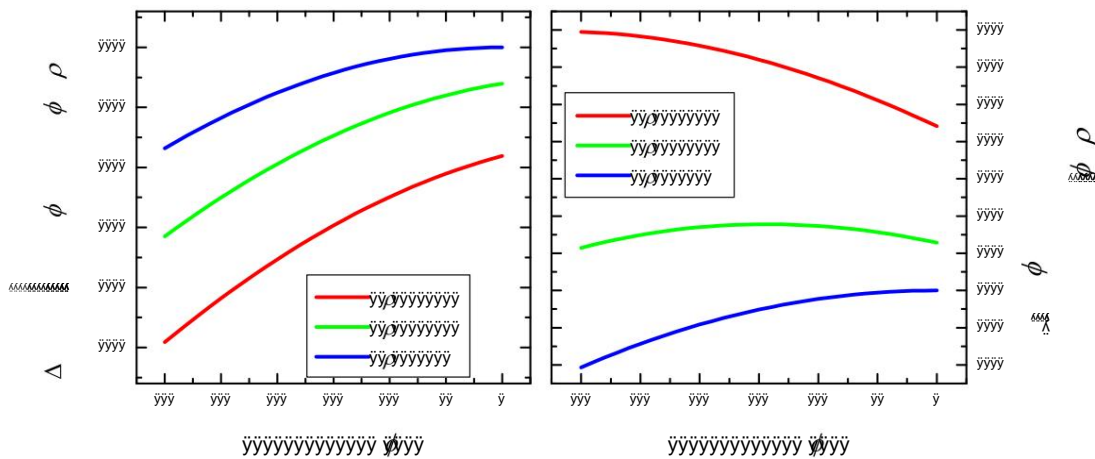


Figure 1.19:

Energy gain at two frequencies and target phase change: On the left, the sum of the energy gains of both linacs is shown in simplified form ($\gamma\gamma\gamma\gamma \ddot{\gamma} \ddot{\gamma}\gamma\gamma\gamma \ddot{\gamma} \ddot{\gamma}$). For $\ddot{\gamma} \ddot{\gamma} \ddot{\gamma}$ the relative energy gain decreases by about 9% - too little for the field gradient. For $\ddot{\gamma} \ddot{\gamma} \ddot{\gamma}\gamma\gamma\gamma\gamma$ it decreases by about 15%, only for $\gamma\gamma\gamma\gamma \ddot{\gamma} \ddot{\gamma} \ddot{\gamma}\gamma\gamma\gamma\gamma$ does it decrease by the amount of 17% required by the field gradient [26]. The ratio $\ddot{\gamma} \ddot{\gamma} \ddot{\gamma} \gamma\gamma\gamma\gamma\gamma\gamma \gamma\gamma\gamma\gamma\gamma\gamma \ddot{\gamma} \ddot{\gamma}\gamma\gamma\gamma\gamma$ is shown on the right. Ideally, $\ddot{\gamma} \ddot{\gamma}$ should be as constant as possible during acceleration, so that the energy gain of one revolution is always distributed approximately equally between both linacs (e.g. green curve for $\ddot{\gamma} \ddot{\gamma} \ddot{\gamma}\gamma\gamma\gamma\gamma$), but changing the energy gain requires $\ddot{\gamma} \ddot{\gamma} \ddot{\gamma}\gamma\gamma\gamma\gamma$.

1.5.5 Coupling between the phase spaces

In certain cases the phase spaces $(x, x\dot{y})$, $(y, y\dot{y})$ and $(\ddot{y}\ddot{y}, \ddot{y}E)$ can be considered independently; Liouville's theorem then applies separately in all three phase spaces. However, the individual subspaces can *no* longer be viewed independently of one another if couplings between the phase spaces occur. Instead, the entire phase space must then be transformed by a 6×6 matrix.

A simple example of this is the shot into the 180° segment magnet of the STM with an angle error $\ddot{y}x\ddot{y} \ddot{y} = 0$. This shortens or lengthens the distance in the magnetic field, so that a phase deviation $\ddot{y}\ddot{y}$ can be observed after the magnet.

However, coupling can also be caused by many other effects and was also occasionally the subject of investigations in the RTMs on MAMI [20, 32].

In the HDMS model developed in Chapter 4, couplings between longitudinal and transverse phase space are deliberately neglected in order not to unnecessarily complicate the model, but the accessible transverse data (usually x, y) are also stored during the measurements carried out.

When analyzing the experiment, for example, those data can then be sorted out

1 The Harmonic Double-Sided Microtron (HDSM)

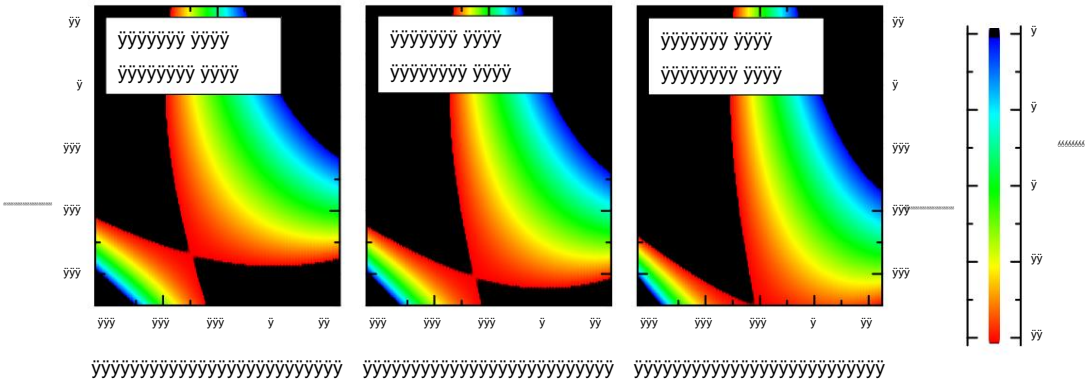


Figure 1.20: Trace of the longitudinal transformation: trace evaluated according to equation 1.38 for three different RF amplitude relations. The acceleration is not stable in the areas shown in black.

which show excessive transversal deviations from the nominal path.

Part II

Beam diagnostics and other systems at MAMI

2 beam diagnostics and other systems

MOMMY

In the previous chapter, it was shown according to which jet dynamic criteria, for example, the target phases ($\varphi_{4.9}$ and $\varphi_{2.45}$) and target amplitudes ($U_{4.9}$ and $U_{2.45}$) of the HDSM were determined. These specifications must now be implemented on the real accelerator in order to enable reliable operation. In addition, it should also be checked which deviations from this target configuration can be tolerated.

A *relative* change in the target *phases* $\varphi_{4.9}$ or $\varphi_{2.45}$ can be effected by actuating a calibrated phase shifter (hereinafter referred to as $\varphi(4.9)$ or $\varphi(2.45)$)—in contrast to the target *phases* $\varphi_{4.9}$ and $\varphi_{2.45}$ —but the absolute magnitudes of $\varphi_{4.9}$ and $\varphi_{2.45}$ as injection phases into the HDSM can only be roughly estimated at first.

Complex HF systems must be controlled

Adjusting the linac amplitudes $U_{4.9}$ and $U_{2.45}$ is even more complicated. The structure of a 4.9 GHz module is shown schematically in Figure 2.1 as an example.

MAMI's control system only specifies an analogue target value for the respective klystron via DAC, each klystron itself is driven by an individual analogue control circuit to the corresponding power. The control circuit itself detects the HF power PHF in the acceleration section. This power is partially dissipated from the section by the acceleration of the beam, so that the HF power to be fed into the section must be corrected by switching the beam on or off (so-called "beam loading") in order to reduce the acceleration voltage (or Linac *amplitudes* $U_{4.9}$ and $U_{2.45}$) to keep constant. The power of certain resonators in an acceleration section can be measured with the help of calibrated HF power meters ("power meter", Section 2.4.1). However, this only allows the acceleration voltage to be estimated, since, for example, the HF power is not evenly distributed over the section ("flatness", [33, 34]). For this reason, the target HF amplitudes are often given in the arbitrary unit EUT in the control system of the accelerator and also in the present work, which only represents the DAC target value of the klystron control.

Requirements for the beam diagnostic systems

Various monitor systems are required to investigate jet dynamic processes and it must be possible to vary the relevant system parameters in a controllable manner.

2 beam diagnostics and other systems at MAMI

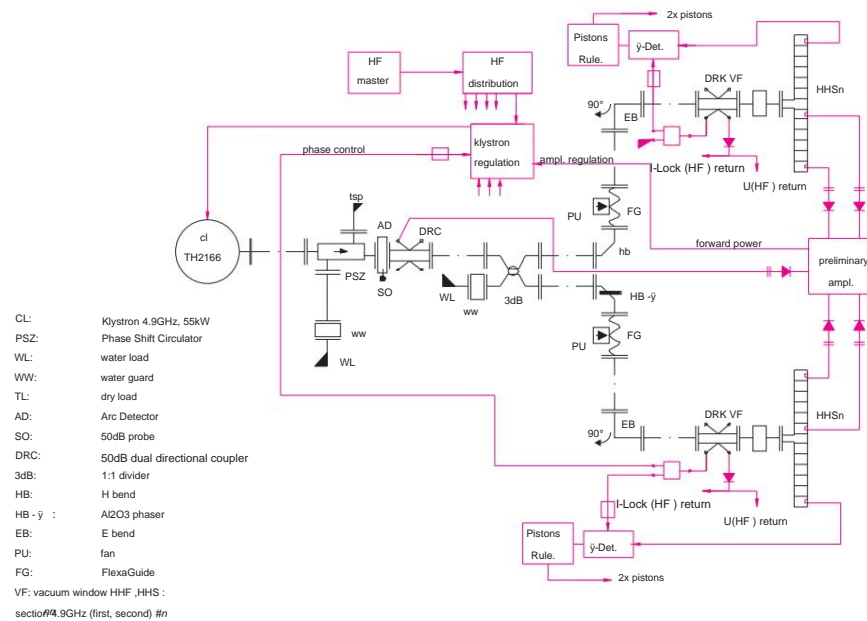


Figure 2.1: HDSM: Schematic of a 4.9 GHz module with different control loops [35].

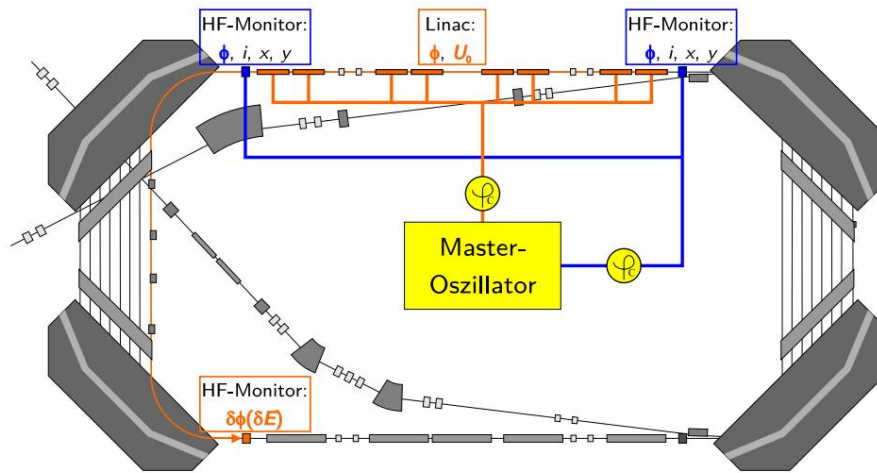
Here, for example, beam positions x should be with a precision of $|\ddot{y}x| < 0.1$ mm or beam phases \ddot{y} with $|\ddot{y}\ddot{y}| < 1\ddot{y}$ resolution can be measured in order to be able to draw meaningful conclusions from these measurements. In order to be able to achieve this, the beam diagnosis systems must be tested and calibrated using suitable methods (eg using waveguide phase shifters). A schematic representation of the systems used is shown in Figure 2.2.

Two classes of beam diagnostic systems

There are two basic differences in beam diagnosis:

- Invasive methods that strongly influence the further course of the beam (or even the disable beam)
- “Non” invasive methods that measure beam properties when measuring beam practically not affect.

In this section, the hardware of the beam diagnosis elements used is presented first, in order to develop the measurement routines based on this in the next chapter.

**Figure 2.2:**

Scheme of the phase measurement in the HDSM: The high-frequency is amplified by the master oscillator (section 2.4.3) at low levels to the HF monitors (section 2.6) and by the klystrons to the sections of both via phase shifters (section 2.4.2). Linacs distributed. The phase shifter of the monitors is used to calibrate and measure the phase signals of the HF monitors (blue). If the shot phase ϕ into the linac is to be determined, the phase shifter of the corresponding linac is used (orange) and the change in phase due to the longitudinal dispersion of the deflection system is exploited to determine the phase of maximum acceleration (ϕ of ϕ) . determine (Section 3.2.2).

For the 2.45 GHz linac, the calibrations and measurements are analogous.

2.1 Invasive Monitor Systems

An invasive monitor system can often be used if the radiation currents required for diagnosis cannot destroy any components. Depending on the question, simple fluorescent screens (position, size), collimators (intensity) or more complex and much more precise wire scanners (position, size) can be used.

2.1.1 Fluorescent screens

The simplest monitor – the fluorescent screen (luminescence monitor, abbreviated: LUMO) – is only suitable to a limited extent in a recirculating accelerator, since the beam is disturbed by the fluorescent screen and further circulations can no longer be achieved. However, the use is quite simple; since the dimensions of such fluorescent screens are known, the image provides direct information about the position and extent of the beam. Fluorescent screens are therefore also well suited to assessing and adjusting the set beam focus (Figure 2.3).

2 beam diagnostics and other systems at MAMI



Figure 2.3: Fluorescent screen with beam spot in the A1 beam path

In the HDSM, however, two fluorescent screens were also mounted on each of the linac axes, in which a hole with a diameter of about 5 mm was drilled in the middle. This makes it possible to accelerate the centered beam with almost no interference and only direct the desired rotation onto the screen. In daily routine, these LUMOs are rarely used because they can also confuse the surgeon (Figure 2.4): Sometimes not only a single beam spot can be seen, but also several "half" beam spots can be seen if the deflected beam is not hits the fluorescent screen completely, so that a partial beam can pass through the LUMO and hit it a second time on the next revolution.

Nevertheless, these LUMOs are also very helpful when diagnosing errors or searching for beams, as they can be used to determine without a doubt whether the beam is reaching the screen or not.

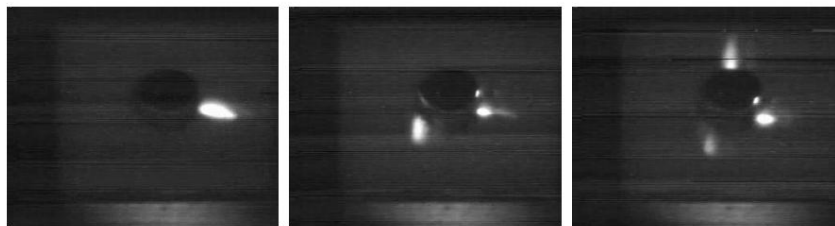


Figure 2.4:

Fluorescent screen in the 2.45 GHz linac: On the left, the beam is completely directed onto the monitor, the image in the middle already shows the second round (bottom left) and the image on the right even shows the third round (above).

2.2 Non-Invasive Monitor Systems

However, many accelerators rely on non-destructive beam diagnostics¹.

Synchrotron radiation monitors for determining the location and shape of the electron beam as well as special high-frequency resonators with which the location, phase or intensity of the beam can be measured have long been tried and tested. These HF monitors are described in detail in Section 2.6, as a large part of the studies on longitudinal dynamics are based on them.

2.2.1 Synchrotron radiation monitors

The analysis of the emitted synchrotron radiation contributes significantly to the understanding of the accelerator. A newly developed system is in use at the HDSM, which can display individual beam spots of individual circuits with a swiveling digital zoom camera. Various studies on transverse emittance have already been carried out with this [36].

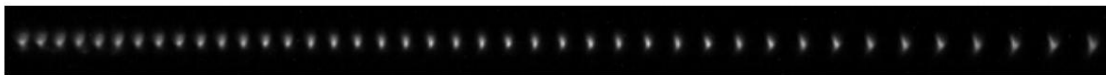


Figure 2.5:

Synchrotron radiation monitor HDSM Dipol 4 (Installation see Figure 1.7): The first orbit is on the right, the last round on the left. The horizontal resolution is 640 pixels [27].

In routine operation, the system allows the transverse matching to be checked in a simple manner. If the beam is *not* adjusted, different sized beam spots of the individual circuits could be seen [32].

The system is not suitable for investigating longitudinal dynamics.

Nevertheless, the transversal matching can be checked in preparation for various measurements. This largely ensures that transverse effects have the least possible influence on the longitudinal phase space, which is assumed in the investigations in Chapter 4. An example of a fitted ray is shown in Figure 2.5.

2.3 Various diagnostic systems

In addition to the fluorescent screens, synchrotron monitors and HF monitors, there are a number of other diagnostic systems on MAMI-C.

¹Extreme examples are synchrotrons, where the temporal development of various disturbances has to be investigated and the beam has to make many revolutions, or on the other hand beam powers in the kW to MW regime, which would immediately destroy any kind of fluorescent screens.

2 beam diagnostics and other systems at MAMI

2.3.1 Förster probe for current measurement

A Förster probe in the 4.9 GHz linac measures the beam current (as in the RTM3). in CW mode with an intrinsic resolution of about $0.2 \mu\text{A}$ [37]. At 43 turns the resolution improves to about 10 nA, which is still a bit worse than in the RTM3 is at 90 rounds². For beam currents greater than $5 \mu\text{A}$, both are correct. Measurements usually agree better than 1%. Figure 2.6 shows the jet current difference over a period of almost two weeks. during this beamtime was typically measured at a beam current of $20 \mu\text{A}$.

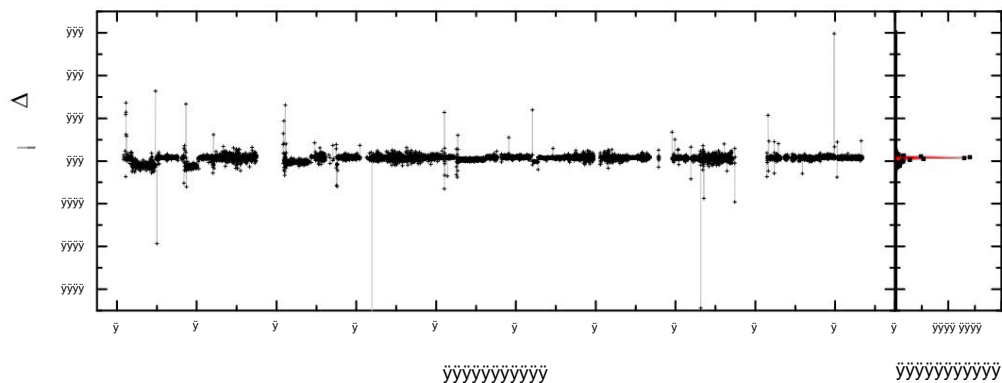


Figure 2.6:
Deviation between Förster probe RTM3 and HDSM at a beam current of 20 A over a Period of 10 days: The full width at half maximum of the histogram is approximately $0.03 \mu\text{A}$.

2.3.2 Ionization probes monitor beam losses

A good 20 ionization probes (IOSOs) comprehensive system for monitoring beam losses is available [38]. This long-standing experience with the IOSOs shows that a good accelerator setting and resulting good beam quality is usually also associated with low indicated beam losses; therefore the probes are also used during optimizations used regularly.

Ten ionization probes are installed at particularly critical points in the HDSM (Figure 2.7). Under favorable circumstances, beam losses of 10 pA are displayed, but beam losses of 1 nA lead to significant ones in any case display values as shown in Figure 2.8. On these instruments is also based

²The beam current in the RTM3 and in the HDSM can only change in the event of a beam loss, even partial differentiate. But then the beam becomes automatic due to the ionization probes (Section 2.3.2). switched off.

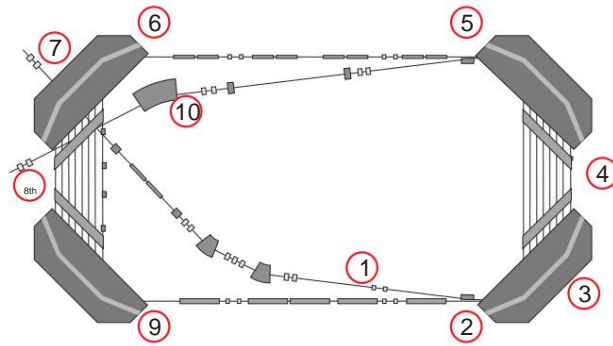


Figure 2.7: Installation of the ionization probes in the HDSM.

the assumption that the relative beam losses at MAMI are typically less than 10^{-5} .

When certain thresholds are exceeded, the interlock system automatically shuts off the beam to reduce the risk of damage or long-term activation of the machine.

Small readings are not always synonymous with lossless acceleration, since the IOSOs cannot indicate every beam loss, eg if the beam is lost in a well-shielded magnetic yoke. However, provided that at least most of the beam reaches the extraction energy, a low-loss setting can be distinguished from a worse one.

2.4 High frequency system

MAMI-C's RF system is a complex setup with different RF levels ranging over 18 orders of magnitude from pW to kW. Normally, control circuits are implemented at low ($< 1\text{W}$) HF levels, while other components (klystron, waveguide, sections) have to be rated in kW

dominate the area.

2.4.1 Accelerating Voltage

A measurement of the high-frequency power PHF of each section, together with the shunt impedance r_{Shunt} , is useful in order to determine the acceleration voltage U_0 of a section or the complete linac according to Equation 2.1. However, both PHF and r_{Shunt} are not easy to measure [39].

$$U_0 = \sqrt{\frac{P_{\text{acc}}}{2 \cdot f_{\text{HF}} \cdot r_{\text{Shunt}} \cdot \text{PHF}}} \quad (2.1)$$

2 beam diagnostics and other systems at MAMI

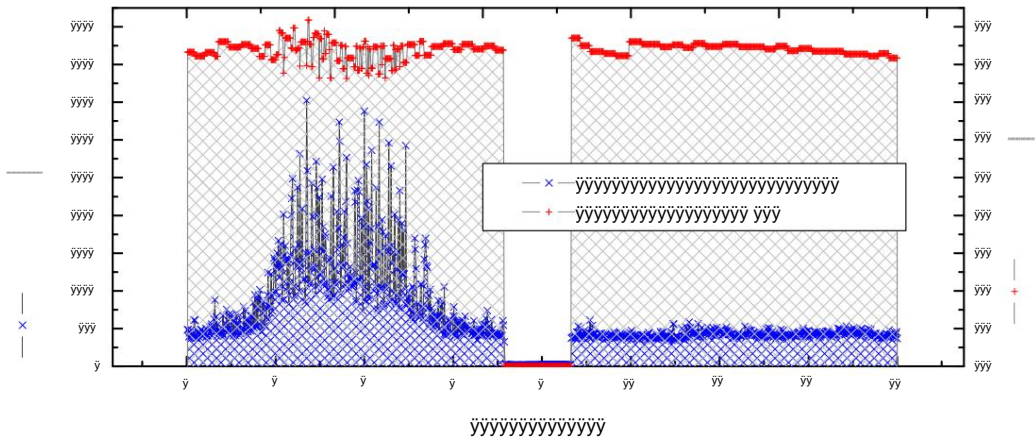


Figure 2.8: Ionization probes in the HDSM show clear radiation levels in the mSv/h range, which correlate with beam losses in the 100 pA range (left area). After an optimization, the radiation levels are significantly lower and the beam current hardly fluctuates; the small jump after about 10 hours was a manual correction of the jet current. In this case, the beam current in the beam stop of experiment (A2) was measured with a Faraday cup.

Quality measurements were carried out during the manufacture of the sections, during which the shunt impedances of the sections were determined. The table below shows the sizes used [34].

	4.9GHz	2.45GHz
Q0	15960	10350 rShunt
	79.6 Mj/m	71.9 Mj/m

Table 2.1: Characteristic data used for the HF sections.

Various methods for measuring PHR are explained below; the Results of all examined methods are compiled in section 3.4.2.

1. HF power meter measurements on the waveguides

The forward power from the klystron to the section can be measured with a calibrated directional coupler and an HF power meter [40].

2. HF diode measurements on the sections All

sections are equipped with diagnostic antennas on four resonators, which decouple a fraction of the electrical fields. These signals will

Fed to RF control systems to control mean RF amplitude (by adjusting klystron power) and mean phase (by piston control to tune resonance). The signal amplitudes are with the above

HF power meter measurements have been calibrated once [40].

3. Calorimetric method

Calorimetry is the second method here to determine the performance of a section. Here, the cooling water flow and its temperature increase measured.

Commercially available water meters are used for the flow measurements, which monitor the cooling water flow of almost all relevant consumers at MAMI. The relevant traffic error limit of these water meters is $\pm 10\%$ for low water flows and $\pm 4\%$ for higher flows. At flow rates of around 100 l/min, the Qn10 meters used are controlled quite well, and it was concluded from redundant test results that the measured water flow rates deviate from each other by only about $\pm 1\%$ [40].

The temperatures in the flow and return of the consumers in question are recorded by Pt100 temperature sensors with a 24-channel measuring device [41] developed at the institute. If the consumers are not switched on, the temperature differences are automatically compared so that possible drifts in the temperature sensors can be corrected as best as possible. During operation, the temperature difference between the flow and return is then measured with an accuracy of better than $\pm 0.1^\circ\text{C}$.

2.4.2 Phase Shifter

Depending on the application, different types of phase shifters are used on MAMI, which can be controlled via the control system.

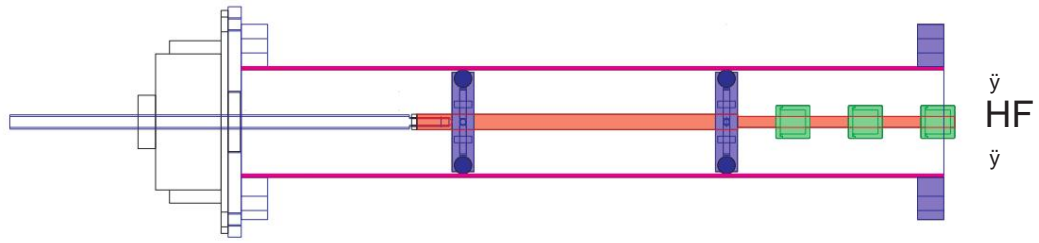
Stepper motor waveguide phase shifter

For precise phase changes over a range of $\pm 250^\circ$, waveguide phase shifters with a stepper motor control are used on MAMI both for 2.45 GHz and for 4.9 GHz (Figure 2.9). The functional principle is based on a choke chain with which an almost contactless short circuit can be precisely positioned in the waveguide [42, 43]. Both versions are suitable for RF levels from milliwatts to kilowatts. The methods presented in Chapter 3 rely to a large extent on the reliability and precision (especially the linearity) of these phase shifters.

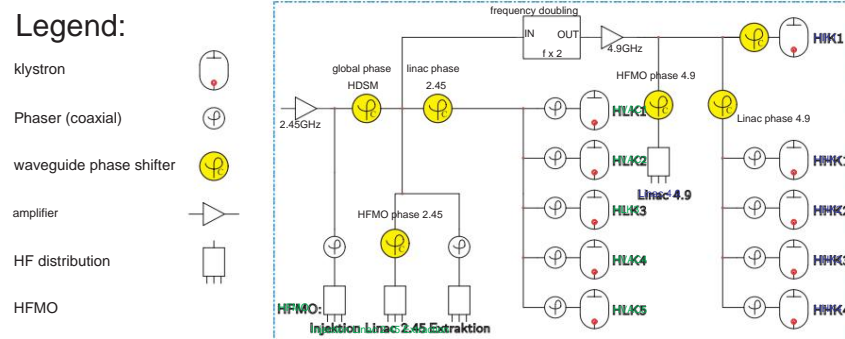
The newly developed phase shifters for 4.9 GHz are essentially a double-frequency optimized copy of the long-established 2.45 GHz phase shifters.

Figure 2.10 shows the phase shifters in the context of the MAMI-C RF installation.

2 beam diagnostics and other systems at MAMI

**Figure 2.9:**

Waveguide phase shifter: The effective length of the waveguide (violet) is changed by a mobile HF short circuit (green) in the form of a choke chain. Due to the interference of the incoming and outgoing HF wave (waveguide flange on the right), this structure can be used as a precision phase shifter, since the short circuit is positioned very precisely by a stepper motor (left). The effective short circuit level is about 2mm behind the first bluff body (green) when looking into the phase shifter. The middle part is used to mechanically guide the short circuit on the long threaded rod (red) [42].

**Figure 2.10:**

MAMI-C: HF distribution with the most important waveguide phase shifters (yellow) [35].

Non-linearities of waveguide phase shifters

Due to the design, the phase shift between the input and output signal should depend linearly on the short circuit position within the waveguide, since the attenuation within the phase shifter is assumed to be constant.

However, there were indications of a non-linear behavior of the waveguide phase shifters from two independent measurement methods: First, the calibration methods from Section 3.1 showed a systematic deviation from the expected linear relationship. However, the commissioning of the autodyne phase measurement (Section 2.4.3) in the HDSM also showed strong deviations from the expected linear relationship between the phase shifter position and the phase shift actually observed.

Both observations gave reason to use each waveguide phase shifter individually

to examine with a network analyzer. Deviations of sometimes more than $\pm 10^\circ$ from the linear progression occurred. The problem is not attributable to the waveguide phase shifters themselves, but to their specific use: low HF levels are normally transported with coaxial cables. In order to use a waveguide phase shifter, the coaxial cable must be connected to the waveguide. However, it is precisely this connection that causes a constant reflection (< 20 dB) that is superimposed on the actual output signal of the phase shifter.

Through individual calibration curves of all phase shifters used, the deviations can be reduced to below 1° (Figure 2.11).

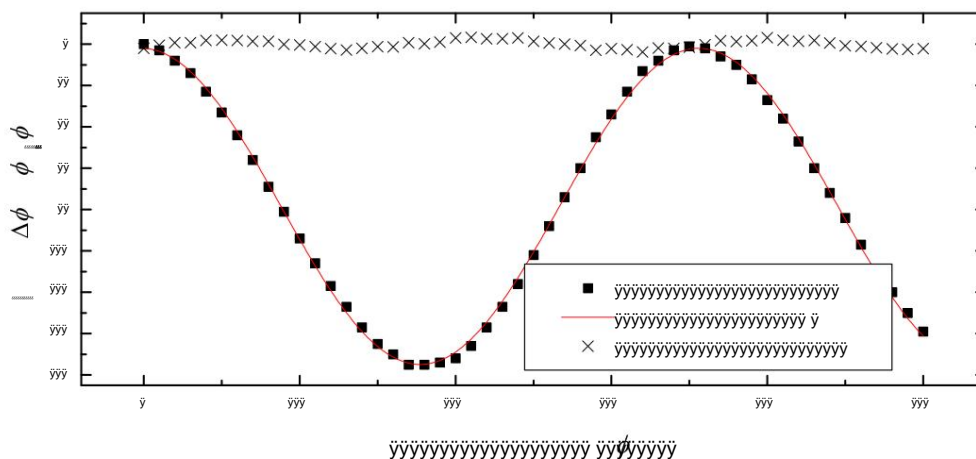


Figure 2.11:

Representation of the deviations from the ideal behavior due to standing wave reflections of a standard 2.45 GHz phase shifter as a function of the target phase. The origin of the ordinate axis is arbitrary. The deviations $\Delta\phi$ after the calibration could be reduced to $\Delta\phi < 1^\circ$.

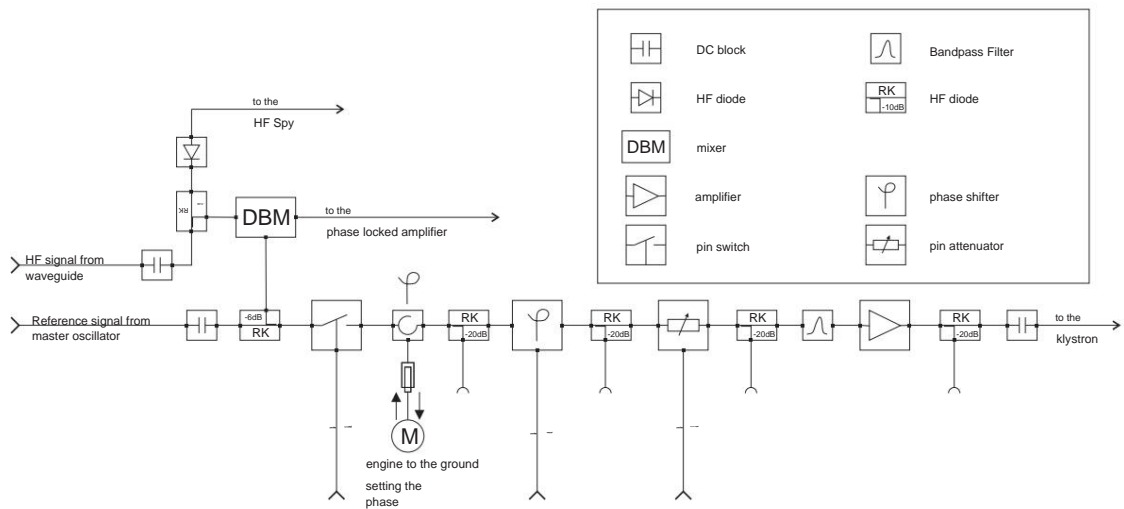
Electronic phase shifters

Mechanical phase shifters are unsuitable for rapid phase variations (eg in the klystron control loops, Figure 2.12). Electronic components are also used here at low power levels. The linearity of these phase shifters is not particularly good and they are therefore poorly suited for systematic measurements (see also Section 3.4.1, Figure 3.14).

Phase shifter control optimization

In the investigations into longitudinal dynamics in Chapter 4, different accelerator configurations are to be set systematically in order to ensure longitudinal dynamics

2 beam diagnostics and other systems at MAMI

**Figure 2.12:**

Schematic of the klystron phase control of an RF module [44]: The interior of the "klystron control" from Figure 2.1 is shown. The phase of the HF signal from the waveguide is compared with the phase of the reference signal using a mixer (DBM) and corrected using an electronic phase shifter (bottom middle).

to study the HDSM. The first thing that matters is high precision. Secondly, the speed plays a role if many different configurations are set during the acceptance measurements and drifts of the accelerator configuration³ are to be avoided due to unnecessarily long measurement times.

The waveguide phase shifters meet the criterion of precision through their calibration. The speed is different: During the measurements, it is necessary to reset one, two or even three of the waveguide phase shifters and then record the signals from the HF monitors. This should take a maximum of one second for the above reasons.

First, the hardware and software of the waveguide phase shifters was examined. The phase shifters are driven at a maximum speed of 100 steps/s (corresponds to about $v_{2.45} = 12 \ddot{y} / \text{s}$ for 2.45 GHz or about $v_{4.9} = 24 \ddot{y} / \text{s}$ for 4.9 GHz). Although the phase shifters can only be operated sequentially, the pure "travel time" to achieve $1 \ddot{y}$ shot phase change⁴ is only $1 \ddot{y} / v_{4.9} + 0.5 \ddot{y} / v_{2.45} \approx 100 \text{ ms}$.

³For example, temperature changes in the cooling water can detune the resonant frequency of the sections or the hall temperature can cause changes in the cable lengths, which can lead to phase changes in HF components. The building technology cannot prevent this completely, but the observed long-term changes hardly interfere with normal experimental operation and can be eliminated by the operator if necessary.

⁴In order to change the HDSM's shot-in phase, the phase shifters of both linacs must be moved around the corresponding amount are driven. More on this in Section 4.2.

In fact, the original program version only achieved times of around 1 s , which was due to generous waiting times in the program. These have been optimized so that the response time of the phase shifters for small phase changes is now less than 100 ms.

In addition, an error in the control could be determined, so that the first step impulse of a route was not processed reliably: After the frequent and short drives during the acceptance measurements (Chapter 4), the initial state of the phase shifters could no longer be reproduced at first and after a subsequent one Calibration trip⁵ reported "lost steps".

In this context, the ADC software for digitizing the HF monitor signals (Section 2.6.5) has also been optimized in order to be able to carry out the computationally intensive signal analysis in parallel with setting the next accelerator configuration (Section 2.7.3).

2.4.3 Autodyne phase measurements

The autodyne phase measurement has been used for a long time as a system for measuring relative phase differences at MAMI [38]. The autodyne phase measurement uses a second reference oscillator, which is about 100 kHz out of tune with the master oscillator , in order to determine the phase information using the resulting intermediate frequency of 100 kHz [45]. In order to determine the phase of a signal in this way , the phase of the master oscillator is mixed down to the intermediate frequency in addition to the HF phase to be measured . This means that there are two signals at 100 kHz whose relative phase shift can be detected much more easily. To do this, the time interval between two zero crossings of both signals is determined, which is possible almost independently of the amplitude of the original HF signals. This fact, as well as a greater precision of the measured phase, are the advantages of the autodyne method compared to the homodyne method used in HF monitors, in which the phase comparison is carried out directly in the baseband.

A measurement channel is provided for each section of the HDSM, so that the phase relative to the master oscillator can be measured independently for all sections. The achievable resolution is 0.1° and better. The system is used in Section 3.4.1 for various measurements.

⁵During a calibration run, the short-circuit slide is moved to a limit switch. If the limit switch is not reached at the expected position, but earlier or later, the original phase was not set correctly, which usually indicates a rare hardware defect.

2.5 Magnetic field measurements

All four HDSM dipoles are operated with separate power supplies. Therefore, all magnets are equipped with their own NMR field probe to measure the field so that a control algorithm can compensate for slow drifts (e.g. due to thermal effects).

Figure 2.13 shows the course of the magnetic field deviations over a typical period of around two weeks.

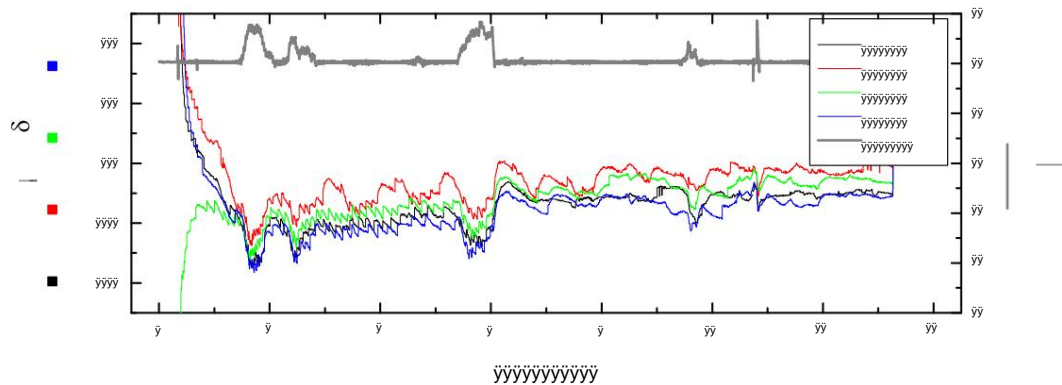


Figure 2.13:

NMR measurement during a 14-day beam time, here at 1604 MeV: The target field of the magnets is about 1.64 T. Deviations are measured by an NMR probe per magnet and corrected by a control algorithm. The cooling water temperature (KW), which has a clear influence on the magnetic fields and thus on the jet dynamics, is shown in gray.

The magnetic field maps recorded during the setup phase (Figure 2.14, [46]) can be used by the tracking program PTRACE [47] to calculate the actual trajectories of the electrons. The energy dependence of the path lengths $s(E)$ can then be described with this path data. The energy and path length pairs determined in this way are used by the HDSM model in Section 4.2 in order to approximate the path length at any energy as well as possible by means of spline interpolation .

Both the temporal stability of the magnetic field (Figure 2.13) and the homogeneity must meet $\delta B/B < 10^{-4}$ (Figure 2.14, right). Larger deviations would result in errors in the deflection angle, which could no longer be corrected by the correction magnets at high energies. Furthermore, the coherence condition according to Equation 1.7 led to changed energy gains and correspondingly large phase deviations when the magnetic field changed. With path lengths in the magnetic field of 4 m to 8 m, a relative change in the magnetic field by 10^{-4} had a linear effect on the actual path length due to the longitudinal dispersion. Thus, path length changes between 0.4 mm and 0.8 mm caused phase changes (to the fundamental frequency of